Search for T-Odd Left–Right Asymmetry of Prompt Neutron Emission in Binary Fission of the ^{233}U and ^{239}Pu nuclei by Slow Polarized Neutrons

G. V. Danilyan*, V. A. Krakhotin*, V. S. Pavlov*, A. V. Fedorov*, E. I. Korobkina**, and E. Lelivre-Berna***

* Institute of Theoretical and Experimental Physics State Research Center, ul. Bol'shaya Cheremushkinskaya 25, Moscow, 117259 Russia
** University of Mainz, Mainz, Germany
*** Laue et Langevin Universite, Grenoble, France
Received October 30, 2000; in final form, November 17, 2000

We report preliminary results of measuring the T-odd left–right asymmetry of prompt neutron emission in binary fission of the ^{233}U and ^{239}Pu nuclei by slow polarized neutrons. Assuming that about 35% of prompt neutrons are emitted from the "neck," one can conclude that the emission asymmetry of scission neutrons in ^{233}U is an order of magnitude lower than the asymmetry of α-particle emission in ternary fission. © *2000 MAIK "Nauka/Interperiodica".*

PACS numbers: 25.85.Ec; 24.80.+y

The T-odd left–right asymmetry recently observed in [1] for the angular distribution of the long-range α particles in ^{233}U and ^{235}U ternary fission by cold polarized neutrons may be caused by electromagnetic or strong interaction in the final state. To establish which of these interactions is responsible for the observed correlation, it is desirable to examine analogous asymmetry for the emission of a neutral particle in ternary fission. However, by ternary fission is historically meant the bipartition accompanied by emission of a light charged particle (LCP). In 90% of events, this is the α particle. The angular distribution of these particles unambiguously attests that they are emitted from the area between the future fragments before the nuclear scission into two fragments. Most models of ternary fission are based on the assumption that LCPs are emitted from the neck connecting "fragments" before its scission. At the same time, it is established experimentally that a portion of prompt neutrons in binary fission are also emitted before nuclear scission. One might naturally consider these neutrons the "neutral" component of nuclear tripartition. Then, if the emission mechanisms are similar for α particles and scission neutrons and if the correlation is due to strong interaction, one can expect the same asymmetry for the emission of scission neutrons. Of course, it should be kept in mind that, contrary to α particles, the neutron spin is nonzero.

The desired left–right asymmetry can be described by the expression

$$W = \text{const}(1 + D_n \mathbf{S}[\mathbf{P}_f \times \mathbf{P}_{sn}]), \qquad (1)$$

where D_n is the asymmetry coefficient, $\mathbf{S}$ is the unit vector along the spin of a neutron captured by the target nucleus, and $\mathbf{P}_f$ and $\mathbf{P}_{sn}$ are unit vectors along the momenta of the light (or heavy) fragment and the α particle, respectively.

Since the electromagnetic interaction of a neutron in the final state is weaker than the interaction of a charged particle, D_n should be much smaller than D_α if the correlation in the ternary fission is due to the electromagnetic interaction.

The first experiment was set up on a polarized thermal-neutron beam from the reactor of the Moscow Institute of Engineering Physics. The geometric arrangement of a target and the fragment and neutron detectors is schematically shown in Fig. 1. The longitudinally polarized neutrons were incident on a target containing 100 μg/cm^2 of ^{233}U on a thin titanium substrate situated midway between two low-pressure multiwire proportional counters spaced 180 mm apart. The plastic scintillator neutron detector with an FÉU-62 photomultiplier was placed outside the fission chamber (filled with hexane to a pressure of 3 torr) at a distance of 220 mm from the target center perpendicularly to the axis of the fragment detectors. The light and heavy fragments were identified by their time of flight from the target to the detectors. The fragment–fragment coincidence pulses triggered a time-to-code converter whose input was fed with pulses from the neutron detector. An example of the time spectrum of neutron–fragment coincidence pulses is shown in Fig. 2. The left peak corresponds to the coincidence between the frag-
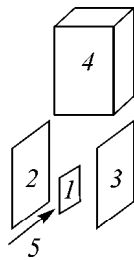
Fig. 1. Geometry of the experiment: (*1*) target; (*2, 3*) fragment detectors; (*4*) fission neutron detector; and (*5*) longitudinally polarized neutron beam.
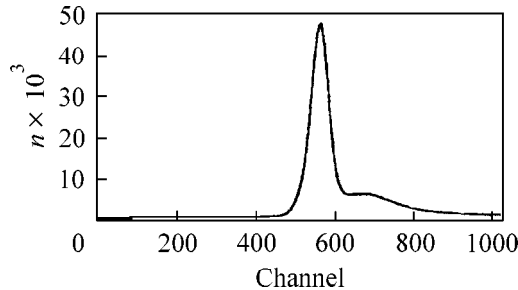
Fig. 2. Time coincidence spectrum. One channel = 100 ps.

ments and the prompt fission γ quanta. A broad time spectrum on the right is caused by the coincidence between the prompt fission neutrons and the fragments. Clearly, a considerable amount of events are due to the neutrons emitted by the fragments. The fragment neutrons in this experiment produce an unwanted background, which, unfortunately, cannot be separated from the events of interest. This background diminishes the absolute value of the asymmetry coefficient by a factor of $(1 + \eta)$, where η is equal to the ratio of the number of detected fragment neutrons to the number of detected scission neutrons. The experimental data on η are quite contradictory: $3 \le \eta \le 35$. However, insofar as the angular and energy distributions of the scission and fragment neutrons are markedly different, it becomes possible not only to correct the experimentally measured asymmetry coefficients for the background but

D_n coefficients measured for the ^{233}U and ^{239}Pu targets

Neutron energy, MeV	Measured D_n values in units 10^{-3}	
	^{233}U	^{239}Pu
<0.7	0.16 ± 0.34	-0.05 ± 0.68
≥0.7	0.35 ± 0.35	0.62 ± 0.53
Prompt γ quanta	0.13 ± 0.15	0.27 ± 0.27

also to determine the η value for the target. The angular distributions of the neutrons emitted by the completely accelerated fragments are concentrated near the fission axis,[1] whereas the emission of scission neutrons is almost spherically symmetric. As regards energy distributions, one can naturally expect that the spectrum of fragment neutrons is "harder" than the spectrum of scission neutrons. Both these factors enable one to estimate the background contribution to the experimental D_n coefficients measured at 90° and 45° (135°) to the mean direction of fission axis. Evidently,

$$D_n(90°)/D_n(45°) = [1 + \eta(45°)]/[1 + \eta(90°)]. \quad (2)$$

The optimum η values satisfying Eq. (2) can be found by the Monte Carlo calculations under reasonable assumptions about the angular and energy distributions of the fragment and scission neutrons, of course, if the desired effect is observed in the experiment, i.e., if it is nonzero.

The second experiment with a ^{239}Pu target was carried out on a beam of polarized 150-meV neutrons from the D3 diffractometer of the Laue and Langevin Institute (Grenoble, France). In this experiment, CF_4 at a pressure of 18 torr was taken as a working gas. The preliminary results of both experiments are presented in the table. No statistically significant effect was observed. Since the D_α value experimentally measured for ^{233}U was found to be 2.7×10^{-3}, it turns out, on the assumption that the contribution of the scission neutrons comprises 35% in this case [2], that the asymmetry coefficient D_n is almost an order of magnitude smaller than D_α. As for ^{239}Pu, the experimental data on the ternary fission of this nucleus are as yet lacking. Of course, measurements will be continued until a statistical accuracy better than 10^{-5} has been achieved.

REFERENCES

1. P. Jesinger, G. V. Danilyan, A. M. Gagarski, *et al.*, Yad. Fiz. **62**, 1723 (1999) [Phys. At. Nucl. **62**, 1608 (1999)]; G. V. Danilyan, A. V. Fedorov, A. M. Gagarski, *et al.*, Yad. Fiz. **63**, 1759 (2000) [Phys. At. Nucl. **63**, 1671 (2000)].

2. N. V. Kornilov, A. B. Kagalenko, and F.-J. Hambsch, ISSIN-**7**, 241 (1999).

Translated by V. Sakun

---

[1] A slightly greater number of neutrons are emitted along the direction of the light fragment.

High-Precision Calculations of the $^{3,1}P_1^o \longrightarrow {}^1S_0$ E1 Amplitudes for Magnesium, Calcium, and Strontium

S. G. Porsev, M. G. Kozlov, and Yu. G. Rakhlina

Konstantinov Institute of Nuclear Physics, Russian Academy of Sciences, Gatchina, St. Petersburg, 188300 Russia

Received November 13, 2000

High-precision calculations of the $^{3,1}P_1^o(nsnp) \longrightarrow {}^1S_0(ns^2)$ E1 amplitudes were carried out for magnesium, calcium, and strontium ($n = 3$, 4, and 5, respectively). The following results were obtained for the reduced matrix element $\langle {}^1P_1^o \| d \| {}^1S_0 \rangle$ of electric dipole moment operator: 4.03(2) au for Mg, 4.91(7) au for Ca, and 5.28(9) au for Sr. These matrix elements are necessary for calculating the van der Waals coefficients C_6, which are used in evaluating the atomic scattering lengths. The latter determine the dynamics and stability of the Bose–Einstein condensate. © *2000 MAIK "Nauka/Interperiodica"*.

PACS numbers: 32.70.Cs; 31.15.Md; 31.25.Jf

In this work, high-precision calculations of the $^{3,1}P_1^o(nsnp) \longrightarrow {}^1S_0(ns^2)$ E1 amplitudes were carried out for magnesium, calcium, and strontium ($n = 3$, 4, and 5, respectively). The computations were motivated by the following reasons. First, in recent years considerable success has been achieved in the development of magneto-optic traps. Trapping and cooling of atoms makes it possible to study the atomic interactions at ultralow temperatures. Most experiments were carried out with alkali atoms, for which it is possible to achieve high densities and low temperatures and observe the Bose–Einstein condensation. However, the interpretation of the experimental data for these systems is quite complicated and ambiguous, in particular, because of the presence of a ground-state hyperfine structure in alkali atoms. For example, the authors of recent works [1, 2] draw antithetical conclusions about the possibility of obtaining the Bose–Einstein condensate for cesium.

An attractive feature of the bivalent atoms is that they have several isotopes with zero nuclear spin. The absence of the hyperfine structure in these atoms facilitates both experimental and theoretical study of atomic interactions. Since the cold traps were already obtained for magnesium, calcium, and strontium, the new possibilities of studying their interatomic interactions and the prospects for achieving the Bose–Einstein condensation of these atoms have been actively discussed, e.g., in [3–5].

The dispersion (van der Waals) coefficient C_6 is one of the main parameters characterizing the dipole–dipole interaction of atoms in a cold trap. This coefficient is necessary for evaluating the atomic scattering lengths, which determine the dynamics and stability of the Bose–Einstein condensate. To calculate the C_6 coefficient, one should know the matrix elements for the E1 transitions from the low-lying odd-parity states to the ground state (see, e.g., [6, 7]). It is worth noting that the expression for C_6 contains the fourth power of matrix elements $\langle {}^{3,1}P_1^o \| d \| {}^1S_0 \rangle$ and, considering the resonant character of the $^1P_1^o \longrightarrow {}^1S_0$ transition (the contribution of the corresponding E1 amplitude to $C_6 \sim 90\%$ [8]), it becomes clear that the E1 amplitude of this transition should be determined with the highest possible accuracy.

Another motive is as follows. Despite the fact that the oscillator strengths and lifetimes of the $^3P_1^o$ and $^1P_1^o$ states were repeatedly determined both theoretically and experimentally [4, 9–12], the results for all three atoms are quite contradictory. In particular, the discrepancies between the data of different experimental groups are as great as 70%. Therefore, high-precision calculations of the above-mentioned E1 amplitudes appear to be well-timed and topical.

We used a method combining the configuration interaction (CI) and the many-body perturbation theory (MBPT). This method was developed by our group over several recent years and successfully applied to the energies of low-lying levels and various observables in some atoms [13]. Since the method is described in detail in the cited papers, we only outline its basic positions. The MBPT is used to construct effective operators (Hamiltonian, electric dipole moment operator, etc.) for valence electrons. In doing so, the interaction between valence and core electrons is taken into account. Next, if the number of valence electrons is two or more, the CI is used to account for the interaction between them. This approach describes both the interaction between valence electrons and the valence–core

correlations and, thereby, improves the accuracy of calculating level energies and various observables by an order of magnitude, as compared to the pure CI method. It should be noted that this method is particularly efficient in the high-precision calculations of bivalent atoms. First, the presence of only two valence electrons allows one to apply full CI. In this case, the number of basis functions is taken to be so large that the error introduced by the incomplete basis set is negligible. Therefore, the problem of unsaturated CI (typical of the systems with many valence electrons) does not arise. Second, due to the compact core, the perturbation series converges better than for the alkali atoms. Because of this, even the second-order MBPT provides a good accuracy for both energies and $E1$ amplitudes.

The aforesaid indicates that the combination of CI and MBPT (CI + MBPT) is highly appropriate for our calculations. We omit the detailed description of the computational procedure (it will be given elsewhere) and pass on to the numerical results for the reduced matrix elements $\langle^{3,\,1}P_1^o\|d\|^1S_0\rangle$ for Mg, Ca, and Sr. For comparison, we present the results obtained for all three atoms by two methods, pure CI and CI + MBPT. In the latter case, we took into complete account the second order and partially included the higher-order MBPT corrections. As regards these latter, the following should be pointed out. Specific to the MBPT for the atoms with several valence electrons, both one- and two- electron diagrams need to be calculated at the step where the second-order corrections to the Hamiltonian are obtained. There are great many of such diagrams ($>10^7$), whose evaluation is a rather time-consuming procedure even for modern supercomputers. Fortunately, there is no need to calculate all the diagrams, and one usually restricts oneself to evaluating several hundred thousand diagrams practically without any loss in accuracy. However, it is clear that an attempt to take into account all the third-order diagrams will face immense technical obstacles and is hardly feasible in practice.

In this connection, a variant with partial inclusion of high-order diagrams in an indirect way seems to be more reasonable. One such method is used in this paper. This method was proposed in [14], where, in particular, it was demonstrated that the agreement between the calculated and experimental spectra of many-electron atoms can be substantially improved by choosing an optimal one-electron Hamiltonian. Below, the optimized effective Hamiltonian is used for calculating the atomic observables. When constructing the effective electric dipole moment operator and at the step of $E1$ amplitude calculations, the RPA equations were solved and one- and two-particle corrections to the RPA were evaluated (including corrections for the normalization of wave functions and for the structural radiation). This procedure is described in detail in [15]. Note that, when solving the RPA equations, we effectively sum a certain subsequence of all-order MBPT diagrams. The RPA equa-

tions were solved at frequency $\omega = E(^1P_1^o) - E(^1S_0)$ for all three atoms. Both length (L) and velocity (V) gauges were used in the calculations. This allowed the control of computational accuracy and was helpful in the estimation of theoretical error. The results are presented in the table.

One can see that the difference between the L- and V-gauge results for the $E1$-allowed $^1P_1^o \longrightarrow {}^1S_0$ transition is 0.3% for Mg, 0.5% for Ca, and 0.8% for Sr. For the $^3P_1^o \longrightarrow {}^1S_0$ transition, the corresponding $E1$ amplitudes are small. This transition is accompanied by a change in the total spin S and, hence, its amplitude is suppressed. Mathematically, this is a result of multiple mutual cancellations of the major contributions that come from the one-electron matrix elements $\langle np_{1/2}\|d\|ns\rangle$ and $\langle np_{3/2}\|d\|ns\rangle$ ($n = 3, 4,$ and 5 for Mg, Ca, and Sr, respectively). This, naturally, impairs the computational accuracy. Nevertheless, the corresponding L- and V-gauge results coincide at a 6% level and are quite satisfactory. The V-gauge matrix element of electric dipole moment operator is written as (atomic units $\hbar = e = m = 1$ are used)

$$\langle f|\mathbf{d}|i\rangle = ic\langle f|\boldsymbol{\alpha}|i\rangle/(E_i - E_f).$$

Here, c is the speed of light, E_i and E_f are the energies of the initial and final states, respectively, and α are the Dirac matrices. Hence, a good result for the V gauge can be obtained if not only the matrix elements of dipole moment operator but also the transition energies are properly calculated. For all three atoms, the $^3P_1^o$, $^1P_1^o$, and $^1S_0$ energies were reproduced with a very high accuracy ($\leq 0.1\%$).

It is worth noting that, for all six transitions (see table), the V-gauge values obtained at the CI step are closer to the final results than the corresponding L-gauge values. Unfortunately, this fact does not imply that the V gauge is more trustworthy in this case. Although the contribution of MBPT to the final result is less for the velocity gauge, this is so because of multiple cancellations of various perturbative corrections, each being several times larger in magnitude than for the length gauge. As a result, the V gauge is much more sensitive to the high-order MBPT corrections than the L gauge. For this reason, the length-gauge values are taken as the final results of our calculations.

Note that the major error in the results is caused by the fact that all-order MBPT cannot be realized. As was mentioned above, the CI is saturated and does not introduce any additional errors. Therefore, the smaller the MBPT corrections, the smaller the resultant error. In addition, the computational error was estimated with allowance made for the proximity of the L- and V-gauge results. The MBPT yields the following corrections to the L-gauge $^1P_1^o \longrightarrow {}^1S_0$ $E1$ amplitudes: 1.6% for Mg, 5.5% for Ca, and 6.4% for Sr (table).

L- and *V*-gauge reduced matrix elements $|\langle^{1,3}P_1^o\|d\|^1S_0\rangle|$ (au) calculated for Mg, Ca, and Sr

Transition	Mg		Ca		Sr	
	CI	CI + MBPT	CI	CI + MBPT	CI	CI + MBPT
$^1P_1^o \longrightarrow {}^1S_0$						
L gauge	4.09	4.03	5.20	4.91	5.63	5.28
V gauge	4.07	4.04	5.11	4.89	5.48	5.32
Resultant value	4.03(2)		4.91(7)		5.28(9)	
Experiment	4.15(10) [9]		4.967(9) [4]		5.57(6) [10]	
	4.06(10) [17]		4.99(4) [10]		5.40(8) [18]	
	4.12(6) [19]		4.93(11) [20]			
$^3P_1^o \longrightarrow {}^1S_0$						
L gauge	0.0055	0.0064	0.027	0.034	0.123	0.161
V gauge	0.0062	0.0062	0.030	0.032	0.133	0.172
Resultant value	0.0064(7)		0.034(4)		0.161(16)	
Experiment	0.0053(3) [21]		0.0357(4) [22]		0.1555(16) [23]	
	0.0056(4) [24]		0.0352(10) [25]		0.1510(18) [25]	
	0.0061(10) [26]		0.0357(16) [27]		0.1486(17) [28]	

The experimental values of matrix elements were obtained by recalculating the $^1P_1^o$ and $^3P_1^o$ levels in the indicated works. (Only those experimental data are presented for which the errors of measurment are the smallest.)

Our final $|\langle^1P_1^o\|d\|^1S_0\rangle|$ values, which can be used for the subsequent calculations (e.g., of the C_6 coefficients), are as follows: 4.03(2) for Mg, 4.91(7) for Ca, and 5.28(9) for Sr. Note that the $^1P_1^o \longrightarrow {}^1S_0$ transition probability in Ca was recently experimentally found to be $2.205(8) \times 10^8$ s^{-1} [4]. Being recalculated to the corresponding transition amplitude, this gives 4.967(9) au. The experimental accuracy of 0.2% is unprecedented for the *E*1 amplitude and far exceeds the accuracy of our calculation. At the same time, this enables us to check the reliability of the estimated computational accuracy. As for Mg and Sr, the accuracy of our results is higher than the experimental accuracy for the former and is at a level of the best experimental results for the latter.

The MBPT contributions to the $^3P_1^o \longrightarrow {}^1S_0$ transitions are considerably greater for the *L* gauge, which we believe to be more reliable than the *V* gauge. In addition, due to multiple cancellations (reaching 99%, e.g., for magnesium) of the major contributions, the role of high-order corrections is much greater for these transitions. In particular, it was demonstrated in [16] that the inclusion of Breit interaction reduces by ~5% the $^3P_1^o \longrightarrow {}^1S_0$ transition amplitude for magnesium. For this reason, we estimate the computational error for this E1 amplitude at a level of 10–12% for all three atoms.

In conclusion, note once more that we have calculated the $\langle^3P_1^o\|d\|^1S_0\rangle$ and $\langle^1P_1^o\|d\|^1S_0\rangle$ matrix elements with emphasis on the high-precision calculations of the singlet–singlet transitions. As expected, the best accuracy is obtained for Mg (0.5%) and it equals 1.4% for Ca and 1.7% for Sr. The accuracy obtained for magnesium is the best in the world, and the results for calcium and strontium are the best among the theoretical works. As pointed out above, the major error in our calculations is due to the incomplete inclusion of high-order MBPT terms. Since the second-order MBPT usually overstates the correlation corrections to various observables, we assume that our results are slightly lower than the true value for the singlet–singlet amplitudes and higher than the singlet–triplet ones. This agrees well with the experimental data on the singlet–singlet amplitudes. One can see in the table that the amplitudes calculated for all three atoms proved to be less than the experimental values. Subsequently, we intend to use the results of this work for calculating the C_6 coefficients for magnesium, calcium, and strontium.

REFERENCES

1. C. Drag, B. Laburthe-Tolra, B. T. Jampens, *et al.*, Phys. Rev. Lett. **85**, 1408 (2000).

2. P. L. Leo, C. J. Williams, and P. S. Julienne, Phys. Rev. Lett. **85**, 2721 (2000).

3. M. Machholm, P. S. Julienne, and K.-A. Suominen, Phys. Rev. A **59**, R4113 (1999).

4. G. Zinner, T. Binnewies, and F. Riehle, Phys. Rev. Lett. **85**, 2292 (2000).

5. T. P. Dinneen, K. R. Vogel, E. Arimondo, *et al.*, Phys. Rev. A **59**, 1216 (1999).

6. A. Derevianko, W. R. Johnson, M. S. Safronova, and J. F. Babb, Phys. Rev. Lett. **82**, 3589 (1999); A. Derevianko and A. Dalgarno, Phys. Rev. A **62**, 062501 (2000).

7. A. Dalgarno and W. D. Davidson, Adv. At. Mol. Phys. **2**, 1 (1966).

8. A. Derevianko, private communication.

9. L. Liljeby, A. Lindgard, S. Mannervik, *et al.*, Phys. Scr. **21**, 805 (1980).

10. F. M. Kelly and M. S. Mathur, Can. J. Phys. **58**, 1416 (1980).

11. T. Brage, C. F. Fisher, N. Vaeck, and A. Gallagher, Phys. Scr. **48**, 533 (1993) and references therein.

12. H. G. C. Werij, C. H. Greene, C. E. Theodosiou, *et al.*, Phys. Rev. A **46**, 1248 (1992).

13. V. V. Dzuba, V. V. Flambaum, and M. G. Kozlov, Phys. Rev. A **54**, 3948 (1996); S. G. Porsev, Yu. G. Rakhlina, and M. G. Kozlov, J. Phys. B **32**, 1113 (1999); S. G. Porsev, Yu. G. Rakhlina, and M. G. Kozlov, Phys. Rev. A **60**, 2781 (1999).

14. M. G. Kozlov and S. G. Porsev, Opt. Spektrosk. **87**, 384 (1999) [Opt. Spectrosc. **87**, 352 (1999)].

15. V. A. Dzyuba, M. G. Kozlov, S. G. Porsev, and V. V. Flambaum, Zh. Éksp. Teor. Fiz. **114**, 1636 (1998) [JETP **87**, 885 (1998)].

16. P. Jonsson and C. Froese Fisher, J. Phys. B **30**, 5861 (1997).

17. L. Lundin, B. Engman, J. Hilke, and I. Martinson, Phys. Scr. **8**, 274 (1973).

18. W. H. Parkinson, E. M. Reeves, and F. S. Tomkins, J. Phys. B **9**, 157 (1976).

19. W. W. Smith and A. Gallagher, Phys. Rev. A **145**, 26 (1966).

20. W. J. Hansen, J. Phys. B **16**, 2309 (1983).

21. A. Godone and C. Novero, Phys. Rev. A **45**, 1717 (1992).

22. D. Husain and G. J. Roberts, J. Chem. Soc., Faraday Trans. 2 **82**, 1921 (1986).

23. D. Husain and J. Schifino, J. Chem. Soc., Faraday Trans. 2 **80**, 321 (1984).

24. H. S. Kwong, P. L. Smith, and W. H. Parkinson, Phys. Rev. A **25**, 2629 (1982).

25. R. Drozdowski, M. Ignasiuk, J. Kwela, and J. Heldt, Z. Phys. D **41**, 125 (1997).

26. C. Mitchell, J. Phys. B **8**, 25 (1975).

27. P. G. Whitkop and J. R. Wiesenfeld, Chem. Phys. Lett. **69**, 457 (1980).

28. J. F. Kelly, M. Harris, and A. Gallagher, Phys. Rev. A **37**, 2354 (1988).

Translated by V. Sakun

(^{139}La, ^{55}Mn) NMR and Magnetic Susceptibility Data on Microscopic Phase Separation in La$_{0.9}$MnO$_3$ Single Crystal

K. N. Mikhalev[1,2], S. A. Lekomtsev[1], A. P. Gerashchenko[1], V. E. Arkhipov[1],
A. V. Korolev[3], Ya. M. Mukovskiĭ[3], and A. A. Arsenov[3]

[1] *Institute of Metal Physics, Ural Division, Russian Academy of Sciences,*
ul. S. Kovalevskoĭ 18, Yekaterinburg, 620219 Russia
[2] *e-mail: mikhalev@imp.uran.ru*
[3] *Moscow Institute of Steel and Alloys, Leninskiĭ pr. 4, Moscow, 117936 Russia*
Received October 13, 2000

Magnetic susceptibility of the La$_{0.9}$MnO$_3$ single crystal was measured and its (^{139}La, ^{55}Mn) NMR spectra were recorded. The data obtained indicate that the areas with an A-type antiferromagnetic order ($T_N = 140$ K) and magnetic moments aligned with the **b** axis occupy a major part of the sample volume in manganite with a considerable concentration of cationic vacancies; simultaneously, the clusters with a canted magnetic sublattice and ferromagnetic interaction between magnetic moments are formed near the vacancies. Charge distribution in these clusters is materially different from that in the antiferromagnetic areas. Magnetic state and relative concentration of the clusters are discussed. © *2000 MAIK "Nauka/Interperiodica".*

PACS numbers: 75.30.Cr; 76.60.-k

Manganites have been extensively studied in recent years because, showing the giant magnetoresistance effect, they offer promise as materials for microelectronics and, at the same time, demonstrate a broad spectrum of physical phenomena caused by the interplay between the orbital, charge, and spin degrees of freedom [1, 2].

The starting LaMnO$_3$ compound is an insulator and, simultaneously, an A-type antiferromagnet with Néel temperature $T_N = 140$ K [3]. This compound can be converted into the metallic state via the heterovalent substitution of bivalent alkaline-earth ions (Ca, Sr, Ba, …) for lanthanum or by increasing the number of vacancies in the cationic sublattice during the course of synthesis.

Two major models lay claim to the explanation of the microscopic properties of manganites. One of them, suggested by de Gennes in [4], predicts a uniform canted magnetic sublattice for LaMnO$_3$ and weakly doped manganites. The other model was proposed in an early work of Wollan and Koehler [3] and recently elaborated by Nagaev in [1]. In this model, the ferromagnetic and antiferromagnetic phases are assumed to coexist in the form of ferromagnetic droplets in an antiferromagnetic matrix. This model has generated the particular interest of researchers in the magnetic and charge states of microareas located near the cationic vacancies or impurity bivalent ions, where a mixture of manganese ions with charges 3+ and 4+ should necessarily occur.

Magnetic neutron diffraction analysis and NMR are most efficient local methods of studying the magnetic state. However, because of fundamental limitations, it seems impracticable to establish the magnetic state of microareas with linear sizes $d < 100$ Å by neutron diffraction, whereas analysis of the NMR data is strongly hampered by inhomogeneous line broadening, short spin–spin relaxation times (see, e.g., [5–8]), and the quality of polycrystalline samples. The single-crystal NMR data for LaMnO$_3$ are presently lacking. At the same time, some nuclei, e.g., ^{139}La ($I = 7/2$) and ^{55}Mn ($I = 5/2$), have quadrupole moments and, thus, interact with the electric field gradient, allowing the local charge distribution to be studied.

In this work, we perform an NMR study of a La$_{0.9}$MnO$_3$ single crystal with the near-percolation-threshold concentration of the presumed ferromagnetic microareas [9].

A La$_{0.9}$MnO$_3$ single crystal was prepared by the floating zone method with radiant heating. The weight of the starting components was chosen so as to account for the technology of crystals with real composition close to LaMnO$_3$. Structural analysis and crystal orientation were carried out on a DRON-type automated X-ray diffractometer equipped with a vacuum chamber for temperature studies with monochromatized Cr K_α radiation.

Magnetic measurements were made on an MPMS-5XL (Quantum Design) magnetometer.
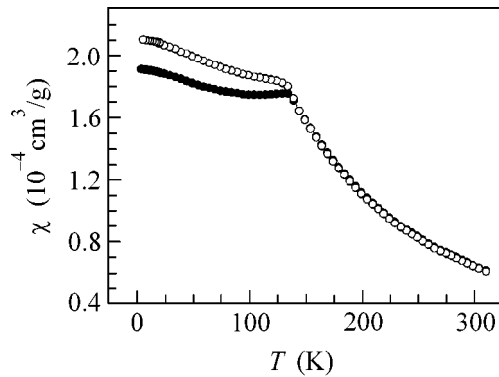
Fig. 1. Temperature dependence of static magnetic susceptibility χ of the $La_{0.9}MnO_3$ single crystal in a magnetic field of 5 T: $\mathbf{H}_0 \parallel$ ($\circ$) $\mathbf{c}$ and ($\bullet$) $\mathbf{b}$.

Fig. 2. Zero-field ^{55}Mn spectra recorded in the ordered state ($T = 4.2$ K) for two different orientations of the alternating rf field about the crystallographic axes of the $La_{0.9}MnO_3$ single crystal: $\mathbf{H}_1 \perp$ ($\bullet$) $\mathbf{b}$ and ($\circ$) $\mathbf{c}$.

The NMR spectra were recorded on a pulsed phase-coherent NMR spectrometer with the quadrature system of signal recording by the integration of spin echo at each frequency point in a zero external field at $T = 4.2$ K (^{55}Mn) and in a field of 9.123 T over the temperature range 85–340 K (^{139}La).

The temperature dependence of magnetic susceptibility is shown in Fig. 1. It increases with decreasing temperature following the Curie–Weiss law, passes through a maximum at the Néel point $T_N = 140$ K, whereupon it becomes orientation-dependent. For a field directed along the presumed direction of magnetic moments in the initial manganite ($\mathbf{H}_0 \parallel \mathbf{b}$), the susceptibility ($\chi_\parallel$) is smaller than for the perpendicular direction ($\chi_\perp$). However, the temperature dependences of $\chi_\perp$ and $\chi_\parallel$ below the Néel point differ from the behavior typical of antiferromagnets (see, e.g. [10]). From these data, one may assume the presence of both a canted magnetic sublattice and a mixture of antiferromagnetic and ferromagnetic phases with a predominance of the antiferromagnetic phase. In this case, one should expect a single ^{55}Mn NMR line with different orientation dependences or two lines.

Indeed, the ^{55}Mn NMR spectra in Fig. 2 are recorded for two different orientations of the alternating field $\mathbf{H}_1$ about the crystallographic $\mathbf{b}$ axis. Each of these spectra shows at least two lines with intensities strongly depending on the sample orientation. It has now been established [11–14] that the signal from the Mn^{3+} ions in the ^{55}Mn NMR spectrum of manganites appears in the frequency range 360–400 MHz, while the Mn^{4+} ions are observed at 300–330 MHz. One usually associates the frequency range between these intervals with a double exchange; i.e., this signal comes from the sample area where the hole mobility is high and the hole lifetime on a manganese atom is shorter than the inverse of the NMR frequency. Although the $\mathbf{H}_1 \perp \mathbf{b}$
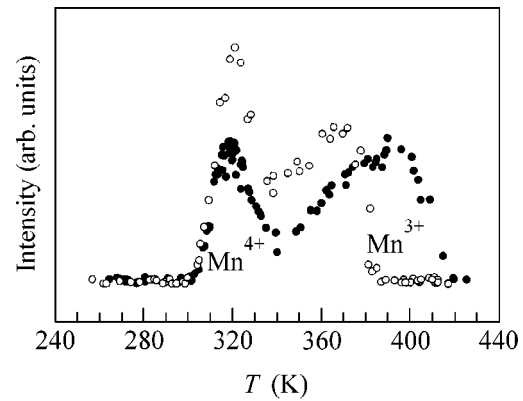
orientation corresponds to the appearance of a signal from Mn^{3+}, nevertheless, both the Mn^{4+} line and a small portion of spectral density in the double-exchange region are also seen. After changing orientation, the Mn^{3+} line intensity sharply decreases, while the Mn^{4+} line becomes stronger. This orientation dependence gives evidence that a part (no less than 50%) of manganese magnetic moments are aligned with the $\mathbf{b}$ axis, which corresponds to the antiferromagnetically ordered tervalent manganese ions; another part is directed at an angle of about 60° to the $\mathbf{b}$ axis and is comprised (judging from the frequency range) of Mn^{4+} ions. Finally, there is a double-exchange region (evidently at the interface) with magnetic moments forming an even larger angle with the $\mathbf{b}$ axis in the manganite under study.

The ^{55}Mn NMR spectrum for the $\mathbf{H}_1 \perp \mathbf{b}$ orientation is closely similar to the spectrum obtained for a polycrystalline $La_{0.8}Ca_{0.2}MnO_3$ [13]. Consequently, the concentration of holes formed through the cationic vacancies in the crystal under study is the same. However, $La_{0.8}Ca_{0.2}MnO_3$ is a ferromagnet with metallic conduction and Curie point $T_C \sim 240$ K, whereas our single crystal is an isolator and an antiferromagnet [9]. It is thus logical to assume that the hole mobility in our initial manganite is appreciably lower due to the cationic vacancies, which function in this case as efficient localization centers.

The typical ^{139}La NMR spectra are presented in Fig. 3 (inset). In both orientations, two lines are clearly visible: a more intense *A* line (~75% relative intensity) with smaller shift and a higher quadrupole frequency (spacing between the quadrupole satellites) of $\nu_Q = 3.4(3)$ MHz and a weaker *F* line with a lower quadrupole frequency of $\nu_Q = 0.7(4)$ MHz. The temperature dependence of line shifts *K* is displayed in Fig. 3. In the
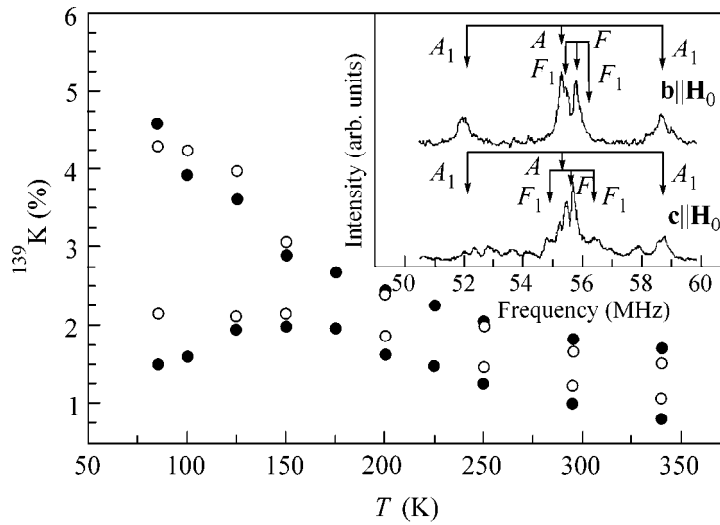
Fig. 3. Temperature-dependent ^{139}La NMR shifts (K) obtained for two orientations of external magnetic field $H_0 = 9.123$ T about the crystallographic axis **b** of the La$_{0.9}$MnO$_3$ single crystal: $\mathbf{H}_0$ ($\bigcirc$) $\perp$ **b** and ($\bullet$) $\parallel$ **b**. The inset shows the typical ^{139}La NMR spectra of La$_{0.9}$MnO$_3$ ($T = 340$ K). A and F indicate the line maxima for the central transitions ($1/2 \longleftrightarrow -1/2$) in the antiferromagnetic and ferromagnetic areas, respectively; A_1 and F_1 are the so-called satellite lines (the first pair corresponds to the $+3/2 \longleftrightarrow +1/2$ transitions).

simplest form, the ^{139}La NMR line shift can be represented as

$$K^{A,F} = (1/\mu_B)H_{hf}\chi_L^{A,F}(T), \qquad (1)$$

where μ_B is the Bohr magneton, H_{hf} is the hyperfine field at the lanthanum, and $\chi_L^{A,F}$ are the local susceptibilities in the sample microareas corresponding, respectively, to the A and F lines. It is reasonable to assume that the hyperfine fields do not depend on temperature so that the temperature dependence of the shift is governed by the behavior of the local susceptibility. In this case, the A-line shift changes with temperature like the susceptibility of a classical antiferromagnet [10]: in the paramagnetic region, the temperature dependences of the local susceptibilities in the external magnetic fields H_0 oriented parallel ($\chi_{\parallel L}^A$) and perpendicular ($\chi_{\perp L}^A$) to the **b** axis are similar; the susceptibilities increase with decreasing temperature to the Néel point $T_N \sim 140$ K; they behave differently in the ordered state: $\chi_{\perp L}^A$ does not change with decreasing temperature, while $\chi_{\parallel L}^A$ decreases. If so, the A line is due to the areas with antiferromagnetic order (Mn^{3+}) and magnetic moments aligned with the **b** axis. This is confirmed by the higher quadrupole frequency and the asymmetry parameter $\acute{\eta} = 0.94(3)$ of the electric field gradient. Both these values are close to the ones previously found for the initial LaMnO$_3$ [8] and satisfactorily agree with the parameters calculated using the point-charge model.

Notice that the shift is slightly anisotropic in the paramagnetic region, presumably because of the presence of a short-range magnetic order in the antiferromagnetic matrix. This is quite conceivable when it is taken into account that, as was proved earlier in [15], the orbital ordering is present in the initial manganite.

The F-line shift increases following the Curie–Weiss law with a decrease in temperature to 85 K. The tendency toward saturation at low temperatures is seen only in the perpendicular orientation. Judging from the large shift and the less steep temperature dependence (the Curie law constant is smaller, as is also the effective magnetic moment), this line corresponds to the ferromagnetically ordered microareas near the vacancies in the cationic sublattice. However, the exchange interaction should be weaker than in the antiferromagnetic matrix, because the Curie temperature, in any case, is lower than 85 K.

The following conclusions can be drawn from this work:

(1) The sample under study consists of the antiferromagnetic matrix (75% relative volume) and ferromagnetic microareas with a canted magnetic lattice and an angle of ~60° between the magnetic moments and the **b** axis.

(2) The charge distribution in the ferromagnetic clusters differs appreciably (judging from the electric field gradient on the lanthanum) from that in the antiferromagnetic matrix and does not fit in the point-charge model. This may be caused either by the local violation of lattice point symmetry in the ferromagnetic clusters near the defects or by the anomalous hole dynamics in these areas.

(3) A small anisotropy of the ^{139}La NMR line shift in the antiferromagnetic matrix is evidence for the presence of a short-range magnetic order in the paramagnetic region, presumably because of the orbital ordering in the initial manganite.

REFERENCES

1. É. L. Nagaev, Usp. Fiz. Nauk **166**, 833 (1996) [Phys. Usp. **39**, 781 (1996)].

2. A. Urushibara, Y. Morimoto, T. Arima, *et al.*, Phys. Rev. B **51**, 14103 (1995).

3. E. O. Wollan and W. C. Koehler, Phys. Rev. **100**, 545 (1955).

4. P.-G. De Gennes, Phys. Rev. **118**, 141 (1960).

5. G. Matsumoto, J. Phys. Soc. Jpn. **29**, 615 (1970).

6. G. Allodi, R. de Renzi, G. Guidi, *et al.*, Phys. Rev. B **56**, 6036 (1997).

7. G. Allodi, R. de Renzi, and G. Guidi, Phys. Rev. B **57**, 1024 (1998).

8. K. Kumagai, A. Iwai, Y. Tomioka, *et al.*, Phys. Rev. B **59**, 97 (1999).

9. N. N. Loshkareva, Yu. P. Sukhorukov, É. A. Neĭfel'd, *et al.*, Zh. Éksp. Teor. Fiz. **117**, 440 (2000) [JETP **90**, 389 (2000)].

10. A. A. Berdyshev, *Introduction to Quantum Theory of Magnetism* (Nauka, Yekaterinburg, 1992).

11. A. Anane, C. Dupas, K. Le Dang, *et al.*, J. Phys.: Condens. Matter **7**, 7015 (1995).

12. P. G. Papavassilion, M. Fardis, M. Belesi, *et al.*, Phys. Rev. Lett. **84**, 761 (2000).

13. Cr. Kapusta, R. C. Riedi, W. Kocemba, *et al.*, J. Appl. Phys. **87**, 7121 (2000).

14. K. E. Sakaie, C. P. Slichter, P. Lin, *et al.*, Phys. Rev. B **59**, 9382 (1999).

15. J.-S. Zhou and J. B. Goodenough, Phys. Rev. B **60**, R15002 (1999).

Translated by V. Sakun

Characteristics of the Magnetic Microstructure of Amorphous and Nanocrystalline Ferromagnets with a Random Anisotropy: Theoretical Estimates and Experiment

R. S. Iskhakov*, S. V. Komogortsev*, Zh. M. Moroz**, and E. E. Shalygina***

* Kirenskiĭ Institute of Physics, Siberian Division, Russian Academy of Sciences,
Akademgorodok, Krasnoyarsk, 660036 Russia

** Siberian University of Routes of Communication, Krasnoyarsk Branch, Krasnoyarsk, 660028 Russia

*** Moscow State University, Vorob'evy gory, Moscow, 119899 Russia

Received October 27, 2000

An experimental determination (both direct and indirect) of the characteristics of the magnetic microstructure, namely, the ferromagnetic correlation radius R_f and the rms fluctuation of the mean anisotropy $D^{1/2}\langle H_a \rangle$, is performed for amorphous and nanocrystalline ferromagnets with a random anisotropy characterized by the quantities R_c and $D^{1/2}H_a$, respectively. The magnetization curves of amorphous and nanocrystalline ferromagnets are found to exhibit a dependence on H that is caused by the alignment of the magnetizations of individual magnetic blocks with the field. © 2000 MAIK "Nauka/Interperiodica".

PACS numbers: 75.30.Gw; 75.50.Kj; 75.60.Ej

1. Amorphous and nanocrystalline ferromagnetic alloys can be represented as an ensemble of clusters or grains of size $2R_c$, which are bound together by the exchange interaction and have randomly oriented easy axes. In the approximation of a continuous medium, such a system is described by the internal energy density

$$U = \frac{1}{2}\alpha(\nabla \mathbf{M})^2 - \frac{1}{2}\beta(\mathbf{Ml})^2 - \mathbf{HM}, \qquad (1)$$

where the magnetization $\mathbf{M}$ is characterized by a constant magnitude M_s, the exchange parameter $\alpha = 2A/M_s^2$ is determined by the exchange interaction constant A, the parameter $\beta = H_d/M_s = 2K/M_s^2$ is determined by the local anisotropy constant K, $\mathbf{l}$ is the unit vector of the easy axis of this anisotropy, and $\mathbf{H}$ is the external magnetic field.

It is known that, in a ferromagnet, an orientational irregularity of the magnetic anisotropy of any origin (crystallographic, elastic, or other) gives rise to the formation of an inhomogeneous state of the magnetic moment $\mathbf{M}(\mathbf{x})$ [1–10]. This state is called in [1, 3] a stochastic magnetic structure (SMS). The parameters of the SMS are determined by the relations between three characteristic fields: the external field H, the exchange field $H_{ex} = 2A/M_s R_c^2$, and the rms fluctuation of the

local anisotropy field $D^{1/2}H_a$, where D is the symmetry factor equal to 1/15 for a uniaxial anisotropy [4]. In the case of large grains satisfying the inequality

$$R_c \geq D^{-1/4}(A/K)^{1/2}, \quad H_{ex} \leq D^{1/2}H_a, \qquad (2)$$

the correlation properties of the inhomogeneous state of the orientation of $\mathbf{M}$ always coincide with the correlation properties of the local anisotropy fluctuations. In this case, the approximation of crystallites without exchange interaction between them is valid. Beginning from the publications [11, 12], this approximation was used for calculating the law of magnetization approach to saturation:

$$\Delta M/M_s = (\sqrt{D}H_a/H)^2, \quad H > D^{1/2}H_a. \qquad (3)$$

For amorphous and nanocrystalline ferromagnets, the other inequality is valid:

$$R_c < D^{-1/4}(A/K)^{1/2}, \quad H_{ex} > D^{1/2}H_a. \qquad (4)$$

If this inequality is satisfied, the correlation properties of the SMS fundamentally differ (in the fields $H < H_{ex}$) from those of the local anisotropy: the deviations of the magnetization $\mathbf{M}(\mathbf{x})$ from the direction of the external field are correlated in space and form a static wave with the characteristic wavelength $R_H = (2A/MH)^{1/2}$. The changes occurring in the correlation properties of the SMS in the vicinity of the field H_{ex} lead to a change in
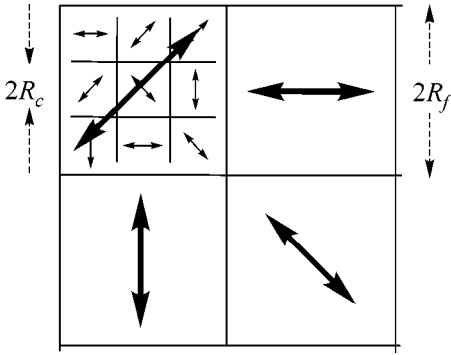
Fig. 1. Schematic representation of a ferromagnet with a random anisotropy. The small arrows indicate random orientation of the local magnetic anisotropy $\mathbf{l(x)}$, and the large arrows show random orientation of the mean anisotropy of a magnetic block $\mathbf{n(x)}$.
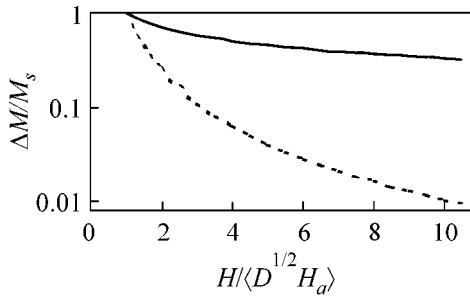
Fig. 2. Theoretical dependences of the variance of magnetic moment on the external magnetic field in the $D^{1/2}\langle H_a\rangle$ units: the solid curve corresponds to Eq. (11) and the dashed curve to Eq. (14).

the law of magnetization approach to saturation. For three-dimensional and isotropic inhomogeneities of anisotropy, the following relationship was obtained [4, 7–9]:

$$
\begin{aligned}
\Delta M/M_s &= (D^{1/2}H_a/H_{ex})^2 (H_{ex}/H)^{1/2} \\
&= (D^{1/2}H_a/H_{ex})^2 (R_H/R_c), \\
&\quad H < H_{ex} \ \text{ or } \ R_H > R_c.
\end{aligned}
\tag{5}
$$

For anisotropic and low-dimensional inhomogeneities, the dependence on H may be different [6, 7, 13–16].

As the magnetic field further decreases ($H \ll H_{ex}$), the situation changes. In low magnetic fields, the magnetic system of amorphous and nanocrystalline ferromagnets exhibits the well-known Imry–Ma effect [17]. This effect consists in the instability of the ferromagnetic state with respect to the randomly oriented local magnetic anisotropy. In this case, the ferromagnetic order is characterized by the correlation length $R_f = R_c(H_{ex}/D^{1/2}H_a)^2$ [5, 10], so that the magnetic structure

of such a material can be described by an ensemble of weakly coupled magnetic blocks (Fig. 1). The block size is $2R_f$, the mean anisotropy in the block is $\langle K\rangle = K/N^{1/2} = K(R_c/R_f)^{3/2}$, and the unit vector $\mathbf{n}$ of this anisotropy is randomly oriented. In the approximation of a continuous medium, such a system can be described by the internal energy density represented in the form

$$
\mathbf{U} = -\frac{1}{2}\beta^e(\mathbf{Mn}) - \mathbf{HM},
\tag{1'}
$$

where the parameter $\beta^e = \langle H_a\rangle/M = 2\langle K\rangle/M^2$ is determined by the constant $\langle K\rangle$ characterizing the mean anisotropy in the magnetic block. In zero field, the magnetization of a magnetic block is oriented along the unit vector $\mathbf{n}$. Therefore, in this case, the correlation properties of the irregular orientation of $\mathbf{M(x)}$ completely reproduce the correlation properties of the fluctuations of mean anisotropy $\langle K\rangle$. This means that the magnetization curve in low magnetic fields should be described by dependence (3) modified as follows:

$$
\begin{aligned}
\Delta M/M_s &= (D^{1/2}\langle H_a\rangle/H)^2 = (R_H/R_f)^4, \\
&\quad H > D^{1/2}\langle H_a\rangle \ \text{ or } \ R_H < R_f.
\end{aligned}
\tag{3'}
$$

Simultaneously, using the definition of the characteristics of the system of magnetic blocks (R_f and $D^{1/2}\langle H_a\rangle$) in terms of the characteristics of the grain system (R_c and $D^{1/2}H_a$), Eq. (5) can be represented in the form

$$
\begin{aligned}
\Delta M/M_s &= (D^{1/2}\langle H_a\rangle/H)^{1/2} = R_H/R_f, \\
&\quad R_c < R_H \ll R_f.
\end{aligned}
\tag{5'}
$$

The aim of our work is the experimental study of the aforementioned effects. Its significance is determined by the fact that the experimental measurement of dependence (3') is a direct, rather than indirect [see Eq. (5')], proof of the existence of magnetic blocks and allows one to directly measure the characteristics of the magnetic microstructure (the quantities $\langle H_a\rangle$, $\langle K\rangle$, and R_f) of amorphous and nanocrystalline ferromagnets.

2. Let us theoretically estimate the correlation properties of the irregular orientation of $\mathbf{M(x)}$. The main characteristic of these properties is the correlation function $K_m(\mathbf{r})$ or the spectral density $S_m(\mathbf{k})$ related to the correlation function through the Fourier transform:

$$
\begin{aligned}
\langle \mathbf{m}_\perp(\mathbf{x})\mathbf{m}_\perp(\mathbf{x+r})\rangle &= K_m(\mathbf{r}); \\
\langle \mathbf{m}_\perp(\mathbf{k})\mathbf{m}_\perp^*(\mathbf{k'})\rangle &= S_m(\mathbf{k})\delta(\mathbf{k-k'}); \\
K_m(\mathbf{r}) &= \int S_m(\mathbf{k})e^{i\mathbf{kr}}d\mathbf{k},
\end{aligned}
\tag{6}
$$

where $\mathbf{m}_\perp(\mathbf{x})$ are the transverse components of the unit vector of magnetization $\mathbf{m(x)} = \mathbf{M(x)}/M$. The magneti-

zation curve is related to $K_m(\mathbf{r})$ and $S_m(\mathbf{k})$ by the standard relationships

$$\Delta M/M_s \equiv d_m(H) = K_m(\mathbf{r})\big|_{\mathbf{r}=0} = \int S_m(\mathbf{k})d\mathbf{k}. \quad (7)$$

The general expression for $S_m(\mathbf{k})$ through the arbitrary spectral density $S(\mathbf{k})$ of the fluctuations of the local anisotropy axis has the form [3, 4, 17]

$$S_m(\mathbf{k}) = \left(\frac{K}{A}\right)^2 \frac{S(\mathbf{k})}{(k_H^2 + k^2)^2}, \quad (8)$$

where $k_H = 1/R_H$ is the wave number of exchange correlations. If we model the stochastic properties of the orientational irregularity of magnetic anisotropy by the simplest correlation function

$$K(r) = De^{-k_c r}, \quad S(k) = \frac{Dk_c}{\pi^2(k_c^2 + k^2)^2}, \quad (9)$$

where $k_c = 1/R_c$, we obtain a symmetric expression for $S_m(\mathbf{k})$:

$$S_m(k) = \frac{1}{\pi^2}\left(\frac{K}{A}\right)^2 \frac{Dk_c}{(k_H^2 + k^2)^2(k_c^2 + k^2)^2}. \quad (10)$$

In this case, the expression for the variance d_m has the form [4]

$$d_m(H) = \frac{(D^{1/2}H_a)^2}{H^{1/2}(H_{ex}^{1/2} + H^{1/2})^3}. \quad (11)$$

One can see that, for $H \gg H_{ex}$, Eq. (11) yields expression (3) for both inequalities (2) and (4) and, for $H \ll H_{ex}$, Eq. (11) yields expression (5).

We now consider a random function $\langle\mathbf{m}(\mathbf{x})\rangle_{R_f}$ that is obtained by averaging the random function $\mathbf{m}(\mathbf{x})$ over the space interval $(\mathbf{x} - |R_f|, \mathbf{x} + |R_f|)$:

$$\langle\mathbf{m}(\mathbf{x})\rangle_{R_f} = \frac{1}{(2R_f)^3}\int_{x-|R_f|}^{x+|R_f|} \mathbf{m}(\mathbf{x})d\mathbf{x}. \quad (12)$$

The stochastic properties of the orientational irregularities of the mean anisotropy $\langle K \rangle$ of magnetic blocks are determined by the rules described in [18]. In the case $R_f \gg R_c$, these properties are described by the correlation function and the spectral density of the following types:

$$\tilde{K}(r) = D\left(\frac{k_f}{k_C}\right)^3 e^{-k_f r}, \quad \tilde{S}(k) = \frac{Dk_f}{\pi^2(k_f^2 + k^2)^2}\left(\frac{k_f}{k_c}\right)^3, (13)$$

where $k_f = 1/R_f$. Substituting Eqs. (13) into Eq. (8) and then into Eq. (7), we obtain the following expression
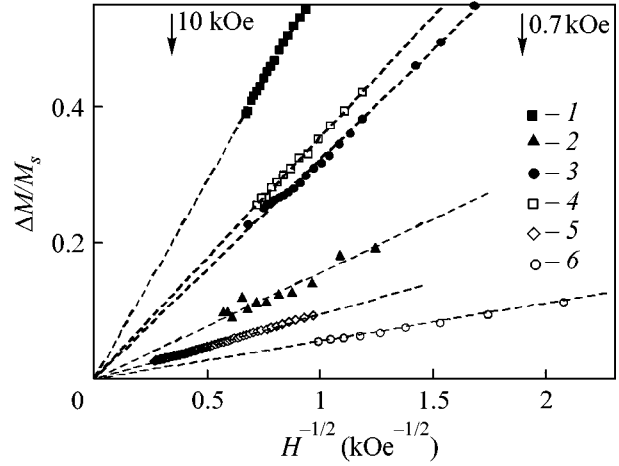
Fig. 3. High-field portions of the magnetization curves $M(H)$: (1) Fe$_{73.5}$Cu$_1$Nb$_3$Si$_{13.5}$B$_9$ and (2) Co$_{80}$Zr$_{10}$ amorphous tapes; (3) a Fe$_{73.5}$Cu$_1$Nb$_3$Si$_{13.5}$B$_9$ nanocrystalline tape; Co$_{90}$P$_{10}$ amorphous films with t = (4) 500 and (5) 2000 Å; and (6) a Co$_{90}$P$_{10}$ amorphous coating with t = 30 μm.

for the variance of the random deviations of $\langle\mathbf{m}(\mathbf{x})\rangle_{R_f}$:

$$d'_m(H) = \frac{(D^{1/2}H_a)^2}{H^{1/2}(H_f^{1/2} + H^{1/2})^3}\left(\frac{R_c}{R_f}\right)^3$$

$$= \frac{(D^{1/2}\langle H_a\rangle)^2}{H^{1/2}(H_f^{1/2} + H^{1/2})^3}. \quad (14)$$

Here, the rms fluctuation of anisotropy in a magnetic block is $D^{1/2}\langle H_a\rangle = D^{1/2}H_a/(R_c/R_f)^{3/2}$ and the field H_f is determined as $H_f = 2A/M R_f^2$. A direct substitution of R_f yields $H_f \equiv D^{1/2}\langle H_a\rangle$. Hence, Eq. (14) is valid only for the fields $H > H_f = D^{1/2}\langle H_a\rangle$. In this field range, Eq. (14) is reduced to Eq. (3'). Figure 2 shows dependences (11) and (14) as functions of magnetic field in $D^{1/2}\langle H_a\rangle$ units. One can see that, up to $H \approx 10D^{1/2}\langle H_a\rangle$, the variations of d_m are insignificant, whereas d'_m drops to zero (within the experimental error). This means that the magnetization of amorphous and nanocrystalline ferromagnets occurs through the alignment of the mean magnetizations of the blocks with the field [according to Eqs. (3') and (14)], and only after that the decrease in the amplitude of $\mathbf{m}_\perp(\mathbf{x})$ [described by Eqs. (5), (5'), and (11)] takes place.

3. Figure 3 presents the high-field portions of the magnetization curves $M(H)$ for films and foils of amorphous and nanocrystalline alloys produced by different techniques (fast quenching of the melt or chemical deposition). The magnetization curves were obtained using vibrating-coil magnetometers with an electromagnet for fields of up to 15 kOe and with a superconducting

solenoid for fields of up to 30 kOe. One can see that, in the $(\Delta M/M_s, H^{-1/2})$ coordinates, the experimental curves can be described by linear dependences (of the type $y = ax$) determined by Eqs. (5) and (5'). This means that inequality (4) is valid for the amorphous and nanocrystalline alloys under study. The experimental curves also suggest that the numerical value of the coefficient of linear dependence is determined by the characteristics of the random anisotropy, R_c and $D^{1/2}H_a$. To calculate the latter, it is necessary to measure the magnetization curve in the fields $H > H_{ex}$. By recording the part of the curve described by dependence (3), one can determine $D^{1/2}H_a$. The revealed crossover of $M(H)$ (the transition from $\Delta M \sim H^{-1/2}$ to $\Delta M \sim H^{-2}$) provides the possibility to measure H_{ex}. Substituting the exchange interaction constant A, which is calculated from the low-temperature thermomagnetic curves $\Delta M \sim (T/A)^{3/2}$, into H_{ex}, one can determine R_c. However, in many cases this program cannot be implemented. Many amorphous and nanocrystalline ferromagnetic alloys are characterized by values of H_{ex} that exceed the maximal fields used in the experimental measurements of $M(H)$ (see, e.g., [16]). Then, the grain size (or the cluster size) $2R_c$ can be determined by direct methods such as X-ray structural analysis or transmission electron microscopy and the values of H_{ex} and $D^{1/2}H_a$ can be calculated (the latter is obtained from the linear dependence $\Delta M \sim H^{-1/2}$ similar to that shown in Fig. 3).

For the characteristics of the magnetic microstructure (R_f and $D^{1/2}\langle H_a \rangle$), the situation is entirely different. For their indirect determination, it is sufficient to record the linear dependences shown in Fig. 3. The measurement of the coefficient of linear dependence allows one to calculate the rms fluctuation of the anisotropy field in a magnetic block, $D^{1/2}\langle H_a \rangle \equiv H_f$. The substitution of A into H_f provides the value of R_f. For the amorphous and nanocrystalline alloys presented in Fig. 3, the following values of $D^{1/2}\langle H_a \rangle$ and R_f were obtained: 340 Oe and 130 Å, respectively, for a $Fe_{73.5}Cu_1Nb_3Si_{13.5}B_9$ amorphous tape 20 μm thick; 25 Oe and 640 Å for a $Co_{80}Zr_{10}V_{10}$ amorphous tape 30 μm thick; 100 Oe and 240 Å for a $Fe_{73.5}Cu_1Nb_3Si_{13.5}B_9$ nanocrystalline tape 20 μm thick; 120 Oe and 380 Å for a $Co_{90}P_{10}$ amorphous film 500 Å thick; 9 Oe and 1430 Å for a $Co_{90}P_{10}$ amorphous film 2000 Å thick; and 3 Oe and 2460 Å for a $Co_{90}P_{10}$ amorphous coating 30 μm thick. To directly determine the values of R_f and $D^{1/2}\langle H_a \rangle$, it is necessary to record the part of the dependence $M(H)$ that is described by Eqs. (3') and (14) rather than by Eqs. (5), (5'), and (11). With a vibrating-coil magnetometer, such a measurement is apparently impossible, because real amorphous and nanocrystalline alloys contain microcracks, pores, and inclusions of a second phase, giving rise to magnetostatic mechanisms of scattering for the magnetic moment [these mechanisms are not included in Eqs. (1) and (1')]. As a result the true values of H

inside the sample do not coincide with the external magnetic field strength at $H \sim H_f$.

This difficulty can be overcome with the use of an experimental technique that allows one to exclude the effect of magnetostatic mechanisms. Such a technique is realized by a magneto-optic micromagnetometer [19] allowing the measurements of the local magnetization curves by using the equatorial Kerr effect $\delta(H) \sim M(H)$ with a light spot diameter of 1 to 30 μm in magnetic fields of up to 200 Oe. In this technique, the external magnetic field is applied along the sample surface normally to the plane of light incidence. Before measuring the local magnetization curves $M(H)$, the system is tuned so as to depart from the significant magnetostatic sources. For this purpose, it is necessary to construct the distribution curves $\delta(L)/\delta_s \sim M(L)/M_s$ at a constant external magnetic field H (much lower than the saturation field H_s). The curves are obtained by scanning the light spot over the sample surface along an arbitrarily chosen direction. (The scan length L is chosen so as to exceed the spot diameter by two to three orders of magnitude.) Typical distribution curves can be found in [20]. They exhibit irregular deviations of M from the mean magnetization $\langle M \rangle$. As the field is increased and the scanning along L is repeated, the value of $\langle M \rangle$ increases and the deviations decrease, but the spatial scale of deviations is retained. The field H_s is determined as the one at which the amplitude of the deviations is of the order of experimental error. For our samples, the following deviations were observed: 200–300 μm for a 500 Å-thick $Co_{90}P_{10}$ amorphous film; 120–150 μm for a $Fe_{73.5}Cu_1Nb_3Si_{13.5}B_9$ amorphous tape; and 50–70 μm for a $Fe_{73.5}Cu_1Nb_3Si_{13.5}B_9$ nanocrystalline tape. The local magnetization curves $M(H)$ were obtained from the light spot, 20–30 μm in diameter, set at the center of a soft magnetic region. It was believed that the deviations of $\mathbf{M}(\mathbf{x})$ in this region are caused by the scattering due to the chaotic orientation of the axis $\mathbf{n}(\mathbf{x})$ of a magnetic block.

Figure 4 shows the local magnetization curves $M(H)$ for a $Fe_{73.5}Cu_1Nb_3Si_{13.5}B_9$ amorphous foil and a $Co_{90}P_{10}$ amorphous film; the curves were measured for different parts of the samples. One can see that, in the $(\Delta M/M_s, H^{-2})$ coordinates, the experimental magnetization curves are described by linear dependences of the type of Eq. (3'). The slopes of these dependences characterize the values of the rms fluctuation of the mean anisotropy field in a magnetic block, $D^{1/2}\langle H_a \rangle$. For the curves presented in Fig. 4, we obtained $D^{1/2}\langle H_a \rangle \approx$ 3–6 Oe and $R_f \approx$ 970–1300 Å for a $Fe_{73.5}Cu_1Nb_3Si_{13.5}B_9$ foil and $D^{1/2}\langle H_a \rangle \approx$ 60–70 Oe and $R_f \approx$ 500–570 Å for a $Co_{90}P_{10}$ film (500 Å thick). One can see that the difference between the values of $D^{1/2}\langle H_a \rangle$ and R_f determined for the $Co_{90}P_{10}$ amorphous film by the direct [Eq. (3')] and indirect [Eq. (5')] methods does not exceed 50%. The greater difference between the corresponding values obtained for a $Fe_{73.5}Cu_1Nb_3Si_{13.5}B_9$ tape is no surprise.
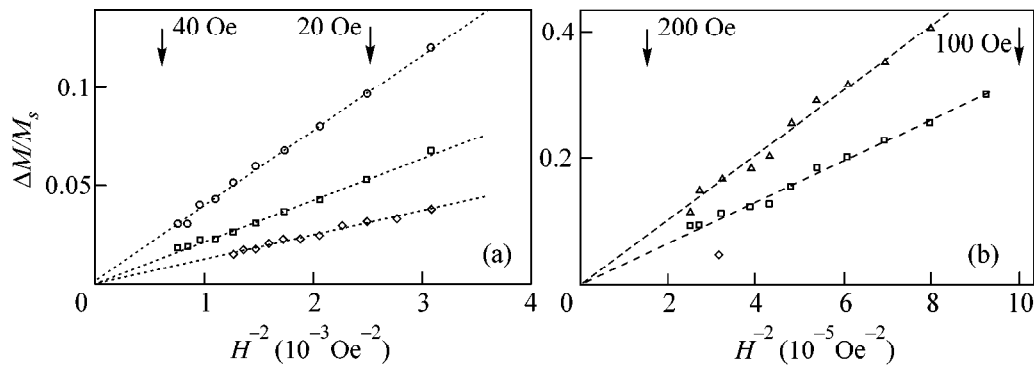
Fig. 4. Local magnetization curves $M(H)$ measured for different parts of (a) a $Fe_{73.5}Cu_1Nb_3Si_{13.5}B_9$ amorphous tape (20 μm) and (b) a $Co_{90}P_{10}$ amorphous film ($t = 500$ Å).

The point is that the local signal $\delta(H) \sim M(H)$ is obtained from a thin surface layer ~200 Å thick. Therefore, a coincidence between the "surface" signal $M(H)$ and the integral value of $M(H)$ should be expected only for films whose thickness is comparable to the penetration depth in the magneto-optic technique. The latter condition is fulfilled for the 500 Å-thick $Co_{90}P_{10}$ amorphous film and does not hold for the foils showing noticeable differences between the values of $D^{1/2}\langle H_a \rangle$ and R_f obtained for the bulk of the samples and for the surface layer of the material.

We are grateful to L.A. Chekanova and V.P. Ovcharov for providing the films and foils and to V.A. Ignatchenko for useful discussions and interest in our study.

REFERENCES

1. H. Hoffman, IEEE Trans. Magn. **2**, 566 (1966).
2. K. J. Harte, J. Appl. Phys. **38**, 1503 (1968).
3. V. A. Ignatchenko, Zh. Éksp. Teor. Fiz. **54**, 303 (1968) [Sov. Phys. JETP **27**, 162 (1968)].
4. V. A. Ignatchenko and R. S. Iskhakov, Zh. Éksp. Teor. Fiz. **72**, 1005 (1977) [Sov. Phys. JETP **45**, 526 (1977)]; V. A. Ignatchenko and R. S. Iskhakov, Izv. Akad. Nauk SSSR, Ser. Fiz. **44**, 1434 (1980); V. A. Ignatchenko, R. S. Iskhakov, and G. V. Popov, Zh. Éksp. Teor. Fiz. **82**, 1518 (1982) [Sov. Phys. JETP **55**, 878 (1982)].
5. R. Alben, J. J. Becker, and M. C. Chi, J. Appl. Phys. **49**, 1653 (1978).
6. H. Kronmüller, IEEE Trans. Magn. **15**, 1218 (1979).
7. A. P. Malozemoff, IEEE Trans. Magn. **19**, 1520 (1983).
8. E. M. Chudnovsky, W. M. Saslow, and R. A. Serota, Phys. Rev. B **33**, 251 (1986).
9. W. M. Saslow, Phys. Rev. B **35**, 3454 (1987).
10. G. Herzer, IEEE Trans. Magn. **26**, 1397 (1990).
11. N. S. Akulov, Z. Phys. **69**, 278 (1931).
12. W. F. Brown, Jr., Phys. Rev. **58**, 736 (1940).
13. E. M. Chudnovsky, J. Magn. Magn. Mater. **40**, 21 (1983).
14. A. G. Chernykh, P. P. D'yachuk, and V. B. Kruglov, Izv. Akad. Nauk SSSR, Ser. Fiz. **53**, 622 (1989).
15. V. A. Ignatchenko and R. S. Iskhakov, Fiz. Met. Metalloved., No. 6, 75 (1992).
16. R. S. Iskhakov, S. V. Komogortsev, A. D. Balaev, *et al.*, Pis'ma Zh. Éksp. Teor. Fiz. **72**, 440 (2000) [JETP Lett. **72**, 304 (2000)].
17. Y. Imry and S.-K. Ma, Phys. Rev. Lett. **35**, 1399 (1975).
18. S. M. Rytov, in *Introduction to Statistical Radiophysics* (Nauka, Moscow, 1966), Part 1.
19. G. S. Krinchik, E. E. Chepurova (Shalygina), and A. V. Shtaĭn, Zh. Éksp. Teor. Fiz. **87**, 2014 (1984) [Sov. Phys. JETP **60**, 1161 (1984)].
20. E. E. Shalygina, L. M. Bekoeva, and A. N. Shalygin, Pis'ma Zh. Tekh. Fiz. **25**, 62 (1999) [Tech. Phys. Lett. **25**, 26 (1999)].

Translated by E. Golyamina

Explanation of Critical Angular Velocities of the Vortex Formation in a Stirred Bose–Einstein Condensate[1]

A. A. Kozhevnikov

Sobolev Institute of Mathematics, Siberian Division, Russian Academy of Sciences,
Universitetskiĭ pr. 4, Novosibirsk, 630090 Russia
e-mail: kozhev@math.nsc.ru
Received November 8, 2000

The problem of explaining the critical angular velocity Ω_c when the formation of a vortex in the stirred Bose–Einstein condensate becomes energetically possible is considered in the framework of the variational approach. The origin of smallness of the calculated Ω_c in comparison with the measured values, which takes place for a pure quantum state with the unit angular momentum per condensed particle, is uncovered. The agreement with the measured Ω_c is achieved upon admitting a small admixture of the zero angular-momentum state in the wave function of the one-vortex quantum state prepared after stirring. A portion of this admixture amounts to 10–13% of the total condensed atoms. A possible test of this hypothesis is proposed. © *2000 MAIK "Nauka/Interperiodica".*

PACS numbers: 03.75.Fi; 05.30.Jp

The Bose–Einstein condensate (BEC) discovered in the trapped clouds of alkali atoms [1] has been proven to be an excellent test site of fundamental concepts of quantum physics of systems consisting of a macroscopically large number of particles [2]. One of the most intriguing features of such systems is the quantized vortex. Recently, the formation of such vortices in the trapped BEC was observed in two different situations. First is the two-component BEC [3], where the vortex state is created via interconversion between two hyperfine states. The second one is realized by the stirring of BEC with a toggled laser beam. This toggling beam creates a small axial asymmetry of the trap potential, which is rotated slowly with the angular velocity Ω. It was found that for Ω exceeding a definite critical value Ω_c, the images of the space distribution of BEC atoms after the ballistic expansion reveal the visible signature of the vortex [4], and even the lattice of the vortex array was observed in some situations [4]. The method of [4] directly corresponds to the classical experiment with the rotating bucket [5]. As was pointed out in [4], the measured critical angular velocity of the formation of a single vortex in the stirred BEC appears to be notably larger than that predicted theoretically [6].

Recently, the efforts aimed at explaining a larger critical angular velocity were undertaken in [7]. The purpose of this work is to propose another explanation of the critical angular velocity Ω_c of the stirring of BEC when the formation of the single vortex becomes energetically possible. To this end, the energy of different configurations of the BEC atoms is calculated. The rea-

son for the smallness of the calculated Ω_c, as compared to the measured one, is revealed. It was shown that the agreement with the measurements can be achieved by assuming the admixture of the vortex-free state with zero angular momentum in the wave function of the final state prepared after the stirring and containment of the visible vortex.

As is known [2], all basic properties of BEC in diluted gases of alkali metals are described by the Gross–Pitaevskii (GP) equation [8] which has the form of Schrödinger equation supplemented with the nonlinear term arising due to the short-range interaction characterized by a single parameter—the scattering length. Since it is the equilibrium energy of the BEC gas that is the main concern here, the GP energy functional

$$E = \int d^3x \left\{ \frac{\hbar^2}{2m} |\nabla \psi|^2 \right.$$

$$\left. + \frac{m}{2} (\omega_\perp^2 r_\perp^2 + \omega_z^2 z^2) |\psi|^2 + \frac{2\pi a \hbar^2}{m} |\psi|^4 \right\} \tag{1}$$

is used instead of the GP equation. In the above equation, $r_\perp^2 = x^2 + y^2$, m is the mass of an atom, $\omega_\perp$ and ω_z are, respectively, the transverse and longitudinal frequencies of the oscillator-like potential modeling the axially symmetric trap, and a is the scattering length. Also, ψ is the condensate wave function normalized according to the condition

$$N = \int d^3x |\psi|^2 \tag{2}$$

---

[1] This article was submitted by the author in English.

and N is the number of condensed atoms. The trap parameters N, $\omega_\perp$, and ω_z are specified as follows. The first set, referred below as the set A, is [4]

$$N = (1.4 \pm 0.5) \times 10^5,$$

$$\frac{\omega_\perp}{2\pi} = 219 \text{ Hz}, \quad \frac{\omega_z}{2\pi} = 11.7 \text{ Hz}, \tag{3}$$

and the corresponding critical angular velocity of stirring is $\Omega_c/2\pi = 152$ Hz [4]. The second set, referred to below as set B, is [9]

$$N = (3.7 \pm 1.1) \times 10^5,$$

$$\frac{\omega_\perp}{2\pi} = 171 \text{ Hz}, \quad \frac{\omega_z}{2\pi} = 10.3 \text{ Hz}, \tag{4}$$

and the corresponding critical angular velocity of stirring is $\Omega_c/2\pi = 115$ Hz [9].

Since the accuracy of determining the number of condensed atoms is about 30% and the energy of BEC is scaled as $E \propto N^{2/5}$ [see [2] and Eqs. (7) and (11) below], it is unnecessary to bother to calculate E with the accuracy better than 10%. So, one may hope that the variational calculation [10] of energy instead of full numerical solution of GP equation will be sufficient. As will soon become clear, it is convenient to take the trial wave function in the form

$$\psi_\kappa(r_\perp, \phi, z) = \left(\frac{N}{\pi^{3/2} R_\kappa^2 z_\kappa} \right)^{1/2}$$

$$\times \left(\sqrt{1 - \kappa} + \sqrt{\kappa} \frac{r_\perp}{R_\kappa} e^{i\phi} \right) \exp\left(-\frac{r_\perp^2}{2R_\kappa^2} - \frac{z^2}{2z_\kappa^2} \right), \tag{5}$$

where $0 \leq \kappa \leq 1$; R_κ and z_κ are variational parameters. Notice that $\kappa = 0$, 1 corresponds to, respectively, the pure vortex-free state and the state with the singly quantized vortex placed at the center of the trap, while intermediate values of κ correspond to an arbitrary mixture of the above states. Introducing the dimensionless parameters ρ_κ and z_κ according to the relations $R_\kappa = (\hbar/m\omega_\perp)^{1/2}\rho_\kappa$ and $z_\kappa = (\hbar/m\omega_z)^{1/2}\zeta_\kappa$, one can find from Eqs. (1) and (5) the energy per condensed atom:

$$\frac{E(\kappa)}{N} = \frac{\hbar\omega_\perp}{2}\left(\frac{1}{\rho_\kappa^2} + \rho_\kappa^2 \right)(1 + \kappa)$$

$$+ \frac{\hbar\omega_z}{4}\left(\frac{1}{\zeta_\kappa^2} + \zeta_\kappa^2 \right) + \frac{\hbar\omega_\perp \gamma_z}{\rho_k^2 \zeta_\kappa}\left(1 - \frac{\kappa^2}{2} \right), \tag{6}$$

where

$$\gamma_z = aN\left(\frac{m\omega_z}{2\pi\hbar} \right)^{1/2}. \tag{7}$$

The mean value of angular momentum in the quantum state with wave function (5) is

$$\langle L_z \rangle = \int d^3x \psi_\kappa^* \left(-i\hbar \frac{\partial}{\partial\phi} \right)\psi_\kappa = \hbar N\kappa. \tag{8}$$

As is known [2, 11], the condition of the thermodynamic possibility of vortex formation in the system rotated at the angular velocity Ω can be formulated as $\Delta E - \langle L_z \rangle \Omega < 0$, where ΔE is the energy difference between the states with the vortex and without it, so that the critical angular velocity is defined as $\Omega_c = \Delta E/\langle L_z \rangle$. Let us evaluate Ω_c in the framework of the variational approach.

The values of variational parameters ρ_κ and ζ_κ can be found from the condition of the minimum of BEC energy (6), which is reduced to the following equations:

$$\rho_\kappa^2 - \rho_\kappa^{-2} = \frac{2\gamma_z(1 - \kappa^2/2)}{\rho_\kappa^2 \zeta_\kappa(1 + \kappa)},$$

$$\zeta_\kappa^2 - \zeta_\kappa^{-2} = \frac{2\omega_\perp \gamma_z(1 - \kappa^2/2)}{\omega_z \rho_\kappa^2 \zeta_\kappa}. \tag{9}$$

First, let us consider the problem of the critical angular velocity in the approximation when the kinetic energy of both the transverse and longitudinal motion can be neglected. This is the Thomas–Fermi (TF) limit [2]. The solution of Eq. (9) in this limit looks as follows:

$$\rho_\kappa^{\text{TF}} = \left[\frac{4\gamma_z^2 \omega_z(1 - \kappa^2/2)^2}{(1 + \kappa)^3 \omega_\perp} \right]^{1/10},$$

$$\zeta_\kappa^{\text{TF}} = \rho_\kappa^{\text{TF}}\left[\frac{\omega_\perp}{\omega_z}(1 + \kappa) \right]^{1/2}. \tag{10}$$
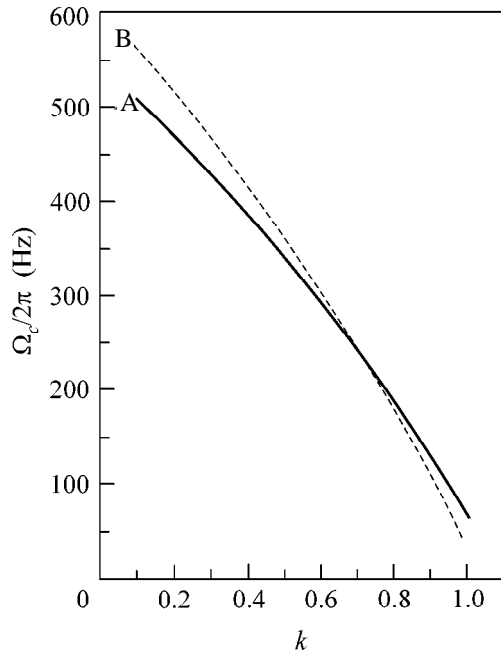
Direct numerical evaluation shows that at, say, $\kappa = 0$ the parameters $\rho_0^{\text{TF}} = 2.16$ (2.63) and $\zeta_0^{\text{TF}} = 9.36$ (10.7) evaluated in this limit for the set of parameters (3) [respectively, Eq. (4)], coincide within the accuracy of 1% with those found from Eq. (9). Hereafter, when doing the specific numerical evaluations, we take the scattering length $a = 5.77$ nm for ^{87}Rb atoms [12] and the above two sets of BEC parameters from Eqs. (3) and (4). The corresponding energy in the TF limit is found to be

$$\frac{E^{\text{TF}}(\kappa)}{N} = \frac{5}{4}\hbar\omega_\perp\left(\frac{4\gamma_z^2 \omega_z}{\omega_\perp} \right)^{1/5} [(1 + \kappa)(1 - \kappa^2/2)]^{2/5}. \tag{11}$$

One can see that in TF limit the energies of the pure vortex-free state ($\kappa = 0$) and the state with a single vortex ($\kappa = 1$) are equal, hence Ω_c found from relation

$$\frac{\Omega_c(\kappa)}{2\pi} = \frac{E(\kappa) - E(0)}{2\pi\hbar N\kappa} \tag{12}$$

{see [2] and Eq. (8)} at $\kappa = 1$ vanishes in the TF limit. Thus, one should take the kinetic energy of the BEC

The critical angular velocity of formation of the quantum state of BEC with one vortex vs. the portion κ of atoms in the state with the unit angular momentum per particle. The curves labeled A and B correspond to the trap parameters in Eqs. (3) and (4), respectively.

Solving Eq. (9) numerically, one can find the energy dependence on κ and calculate the critical angular velocity from Eq. (12). The result of this calculation is shown in the figure. Then, fitting the calculated critical angular velocity (12) to the experimental values is possible if the portion κ of the number of BEC particles in the state with the unit angular momentum per particle amounts to, respectively,

$$\kappa^A = 0.87, \quad \kappa^B = 0.90. \tag{13}$$

The latter values, in view of Eq. (8), give, respectively, $\langle L_z \rangle / N = 0.87\hbar$ and $0.9\hbar$ and do not contradict the measured magnitude [9] of the mean angular momentum of the condensate. Equation (13) means that the admixture of the atoms in the zero angular-momentum state in the case of the trap parameters (3)–(4) amounts to 0.13 (0.1), respectively. Notice that, despite the essential difference in the experimental trap parameters (3) [4] and (4) [9], the portion of the number of atoms in the zero-momentum state needed to explain very different observed critical angular velocities in the final state prepared after the stirring turns out to be practically the same. To be more precise, the 30% accuracy of determining the number of atoms in the condensates reported in [4, 9] implies, as is explained earlier in this paper, approximately 10% uncertainty of the calculation of energy per condensed atom, which translates to approximately the same uncertainty of calculation of κ, while the central values of the calculated κ differ in the above experimental conditions by 3–4%, which is well below their estimated uncertainty.

Could the proposed feature of the BEC wave function such as the presence of the portion $1 - \kappa$ of zero angular-momentum-condensed atoms be tested in experiments? Let us discuss this issue. As is known [4, 9], the presence of the vortex is detected through the visualization of the images of the BEC cloud obtained after its ballistic expansion. One can obtain the spatial distribution of the BEC atoms after this expansion by the usual quantum mechanical method upon finding the wave function (5) in the momentum-space form, propagating it forward in time freely, and then finding its resulting coordinate-space form. The resulting spatial distribution appears to be

cloud into account. Here, this is done by the numerical solution of Eq. (9) for the two values $\kappa = 0, 1$. The result is $\rho_0 = 2.19$ (2.64), $\zeta_0 = 9.28$ (10.66), and $\rho_1 = 1.61$ (1.90), $\zeta_1 = 9.06$ (10.53) in the case of experimental conditions (3) and (4), respectively. One then finds $\Omega_c^A / 2\pi = 65.9$ Hz and $\Omega_c^B / 2\pi = 36.1$ Hz, where the upper indices refer to the two above sets of the trap parameters. The smallness of these values, as compared to those experimentally measured, is due to the smallness of the energy difference between the pure BEC states with $\kappa = 0$ and 1.

To reconcile the result of calculations with the measurements in the present approach, one should keep in mind that, in fact, the density of atoms does not vanish in the central dip [4]. The authors of [4] propose three possible reasons for this: (i) oscillations of the vortex filament, (ii) the presence of noncondensed atoms, and (iii) insufficient resolution of the imaging optics, as compared to the vortex core radius of the BEC cloud. Here, I propose the fourth possible reason and admit that the quantum state of the BEC cloud after the stirring is the superposition of pure quantum states with the angular momenta per particle $L_z/N = 0$ and $\hbar$, that is, admitting $\kappa \neq 1$ in the wave function (5) of the final quantum state. The presence of BEC atoms in the state with zero angular momentum explains in a natural way a nonzero density in the central dip.

$$\rho(r_\perp, \phi, z, t) = \frac{N}{\pi^{3/2} R_\kappa^2 z_\kappa} \left(1 + \frac{\hbar^2 t^2}{m^2 z_\kappa^4}\right)^{-1/2} \left(1 + \frac{\hbar^2 t^2}{m^2 R_\kappa^4}\right)^{-1}$$

$$\times \exp\left[-\frac{r_\perp^2}{R_\kappa^2 + \left(\frac{\hbar t}{m R_\kappa}\right)^2} - \frac{z^2}{z_\kappa^2 + \left(\frac{\hbar t}{m z_\kappa}\right)^2}\right]\left[1 - \kappa \tag{14}\right.$$

$$+ \frac{\kappa r_\perp^2/R_\kappa^2 + 2\sqrt{\kappa(1-\kappa)}\,r_\perp\left(\cos\phi + \dfrac{\hbar t}{mR_\kappa^2}\sin\phi\right)/R_\kappa}{1 + \left(\dfrac{\hbar t}{mR_\kappa^2}\right)^2}\Biggr].$$

One can see that the dependence of the spatial distribution of the BEC atoms on the azimuth angle ϕ is the signature of the above admixture of the vortex free state. The dependence arises from the interference term. But the contribution of the latter becomes significant only after some duration of the process of free expansion. Taking the estimates of the rms values of $r_\perp/R_\kappa$ and $r_\perp^2/R_\kappa^2$ from the written spatial distribution function, one can find that the axial asymmetric contribution $\propto \sin\phi$ becomes dominant after the time of flight

$$t > \tau \approx \frac{mR_\kappa^2}{\hbar}\sqrt{\frac{\kappa}{2(1-\kappa)}}. \tag{15}$$

Using the parameter sets in Eqs. (3) and (4) and the results of numerical solutions of Eq. (9), together with Eq. (13), one can find from Eq. (14) that the interference term becomes dominant after a free expansion time exceeding $\tau = 24$ ms (50 ms), respectively. Since the time of free expansion reported in [4, 9] is 27 ms, it is clear that the proposed feature of the final wave function that could emerge after the stirring had no time to develop in the experiments [4, 9]. An additional testable feature of the proposed wave function of the final state is the flattening of the central vortex dip in the density distribution, due to the increasing relative contribution of the zero angular-momentum state $\propto 1 - \kappa$ as time of free expansion of the BEC cloud increases. It would be interesting to enlarge (if possible) the time of ballistic expansion of the BEC clouds after the stirring to see whether the dependence of their spatial distribution will acquire the angular dependence $\propto \sin\phi$ and to study the relative weights of the components of condensed atoms with different angular momentum at different times of their ballistic expansion.

REFERENCES

1. M. H. Anderson, J. R. Ensher, M. R. Mathews, *et al.*, Science **269**, 198 (1995); K. B. Davis, M.-O. Mews, M. A. Joffe, *et al.*, Phys. Rev. Lett. **74**, 5202 (1995); C. C. Bradley, C. A. Sackett, J. J. Tollet, and R. G. Hulet, Phys. Rev. Lett. **75**, 1687 (1995).

2. F. Dalfovo, S. Giorgini, L. P. Pitaevskii, and S. Stringari, Rev. Mod. Phys. **71**, 463 (1999).

3. M. R. Mathews, B. P. Anderson, P. C. Haljan, *et al.*, Phys. Rev. Lett. **83**, 2498 (1999).

4. K. W. Madison, F. Chavy, W. Wohlleben, and J. Dalibard, Phys. Rev. Lett. **84**, 806 (2000); cond-mat/0004037.

5. W. F. Vinen, Nature **181**, 1524 (1958); E. J. Yarmchuk, M. J. V. Gordon, and R. E. Packard, Phys. Rev. Lett. **43**, 214 (1979).

6. E. Lundh, C. J. Pethick, and H. Smith, Phys. Rev. A **55**, 2126 (1997).

7. J. J. Garcia-Ripoll and V. M. Pérez-Garcia, cond-mat/0006368; A. A. Svidzinsky and A. L. Fetter, cond-mat/0007139; D. L. Feder, A. A. Svidzinsky, A. L. Fetter, and C. W. Clark, cond-mat/0009086.

8. E. P. Gross, Nuovo Cimento **20**, 454 (1961); L. P. Pitaevskii, Zh. Éksp. Teor. Fiz. **40**, 646 (1961) [Sov. Phys. JETP **13**, 451 (1961)].

9. F. Chevy, K. W. Madison, and J. Dalibard, Phys. Rev. Lett. **85**, 2223 (2000).

10. G. Baym and C. J. Pethick, Phys. Rev. Lett. **76**, 6 (1996); D. L. Feder, C. W. Clark, and B. I. Schneider, Phys. Rev. Lett. **82**, 4956 (1999).

11. E. M. Lifshitz and L. P. Pitaevskiĭ, in *Course of Theoretical Physics*, Vol. 5: *Statistical Physics* (Nauka, Moscow, 1978; Pergamon, New York, 1980), Part 2, Chap. III.

12. H. M. J. M. Boesten, C. C. Tsai, J. R. Gardner, *et al.*, Phys. Rev. A **55**, 636 (1997).

Large Magnetoresistance in an Inhomogeneous Magnetic Semiconductor

N. I. Solin and S. V. Naumov

Institute of Metal Physics, Ural Division, Russian Academy of Sciences,
ul. S. Kovalevskoĭ 18, Yekaterinburg, 620219 Russia
e-mail: suhorukov@imp.uran.ru
Received November 9, 2000

A new way of attaining large values of magnetoresistance in a magnetic semiconductor was investigated. The mechanism of magnetoresistance is based on the formation of a space charge, a depletion layer, and a contact potential U_c at the interface between two semiconductors with different Fermi levels E_n^F and E_p^f and on the dependence of U_c, the electrical resistivity, and the size of the depletion layer in the magnetic semiconductor on the magnetic field strength. The model proposed was experimentally verified using a microstructure consisting of an $HgCr_2Se_4$ n-layer with a thickness of up to several tens of microns deposited on the surface of a bulk p-$HgCr_2Se_4$ single crystal. Depending on microstructure parameters, a sharp (up to ~ 30 times) rise in the current flowing through the n-layer was observed in the region of Curie temperature upon switching on a magnetic field ($H \sim 15$ kOe). © 2000 MAIK "Nauka/Interperiodica".

PACS numbers: 72.20.My; 73.25.+i; 73.40.-c

Elucidation of the nature of magnetoresistance (MR) in magnetic materials such as superlattices, magnetic semiconductors, and lanthanum manganites is a practically important and topical problem of modern physics. The highest MR values (as high as $10^{11}\%$) were found in magnetic semiconductors [1, 2]. The known MR mechanisms in magnetic semiconductors, namely, intersection of the impurity and conduction bands, magnetic polarons, ferrons, phase separation, etc. [1], qualitatively explain but provide no answer to the question of how to fabricate materials with large MR values. Because of this, large MR values in magnetic semiconductors are observed for "occasional" samples, whereas the mechanisms of their variation under the conditions of fabrication of such materials are unknown. The situation is very similar for lanthanum manganites. The colossal magnetoresistance ($\approx 10^6$–$10^8\%$) in lanthanum manganites is mainly observed for films or superlattices [3]. The MR values in perfect bulk single-crystal lanthanum manganites are not so high and, apparently, can be understood within the double exchange model with allowance made for the cascade of structural and phase transitions, charge and orbital ordering, and other properties characteristic of perovskites [4]. The aforesaid stimulates a search for other mechanisms of magnetoresistance.

It is known [5] that the unreliability and ambiguity of many results obtained in early investigations of classical semiconductors were connected with the inability to separate the bulk effects from the surface effects or from the effects of the interface between substances differing in nature and with the fact that the overwhelming majority of semiconductor applications were based on the surface and contact phenomena. In [6], we explained the kinetic features and MR of polycrystalline manganites by the surface contact phenomena. We believed that there exists a layer on the grain surface with properties slightly differing from the properties of the sample inside the grain. Such a layer is usually formed, for example, in ferrites [7], because there is no equilibrium between the atmosphere and the sample during the course of its preparation. It was suggested that the nature of magnetoresistance is associated with the formation of a space charge, a contact potential, and a depletion (barrier) layer at the interface between the surface layer and the grain bulk and with the dependence of the contact potential on the magnetic field strength. Based on the dc current and microwave studies of the manganite magnetoresistance as a function of temperature and electric field (breakdown) strength, we estimated [6] the thickness of the inhomogeneous surface layer ($\approx 10^{-5}$ cm) and the potential barrier height ($U_c \approx 0.05$ eV) between the surface layer and the grain bulk. In support of these suggestions, this work presents a model and experimental evidence of the effects of inhomogeneous states ("phase separation") and surface and contact phenomena on the magnetoresistance in magnetic semiconductors.

Interface model of colossal magnetoresistance. A thin, well-conducting film of a magnetic semiconductor with thickness τ_n is placed on the surface of a poorly conducting magnetic semiconductor of thick-

ness τ_p (Fig. 1), with Fermi levels E_n^F and E_p^F. In the limiting case, these are p- and n-type semiconductors. An equilibrium between the semiconductors [5] is established through the diffusion of electrons from the n region to the p region and holes to the n region. On bringing these films into contact, a space charge is formed at the interface, and a contact potential $U_c = E_n^F - E_p^F$ arises equal to the difference between the Fermi levels of the p and n films. The number of electrons that must pass from the n region to the p region when the semiconductors are in contact at the distance d can be estimated as [5]

$$n_d = U_c \varepsilon_0 / e d. \qquad (1)$$

When the semiconductors are in direct contact at the interatomic distance $d = 5 \times 10^{-8}$ cm, the number of diffusing electrons equals $n_d \approx 2 \times 10^{13}$ cm^{-2} for the dielectric constant $\varepsilon_0 = 10$ and $U_c = 0.2$ eV. An atomic layer of a semiconductor with an impurity concentration $N = 10^{15}$ cm^{-3} contains $n_s = (10^{15})^{2/3} = 10^{10}$ cm^{-2} electrons. Thus, the boundary layers d_n and d_p (up to 1000 atomic layers) of the semiconductors are depleted in electrons. A layer of an appreciable thickness $d_L = d_n + d_p$ (up to tens of microns, depending on the parameters of the semiconductor) becomes nonconducting because of a decrease in the concentration of carriers in the barrier layer by a factor of the order of $\exp(U_c/T)$. For example, at $U_c = 0.2$ eV and temperature $T = 100$ K, the charge carrier concentration in the barrier layer must decrease by a factor of more than 10^9.

On bringing these films into contact, the electrical resistivity of the n layer increases (or, more precisely, the current flowing through the n layer decreases) because of the following (Fig. 1):

(1) a decrease in the volume of the conducting layer if the film thickness τ_n is comparable to the thickness of the space-charge layer d_n, $\tau_n \geq d_n$;

(2) a decrease in the concentration of charge carriers in the barrier layer if $\tau_n < d_n$.

Strong variations of the band structure parameters E^F and U_c as functions of the magnetic field strength are a characteristic property of magnetic semiconductors. The greatest changes in the absorption edge ("red shift") in a magnetic field are observed in the vicinity of the Curie temperature T_C and are of the order of $dU/dH = 5{-}10$ meV/kOe in ferromagnetic semiconductors like EuO and HgCr$_2$Se$_4$ [8]. In a magnetic field, the contact potential decreases, leading to a negative magnetoresistance. Therefore, even in relatively low magnetic fields of ~ 10 kOe, the barrier layer may become enriched, $U_c = 0$, and the electrical resistivity of the n film sharply decreases, almost attaining its initial value.

Experiment. To verify the model proposed, we created n-HgCr$_2$Se$_4$ layers on the surface of a p-type HgCr$_2$Se$_4$ single crystal. The layers were of approxi-
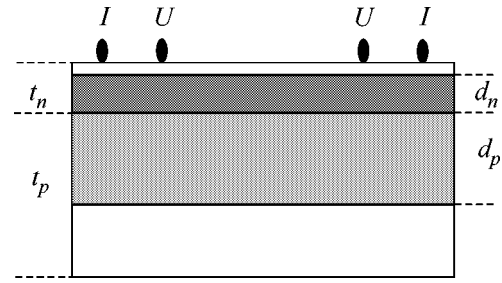

Fig. 1. Scheme of a contact structure for n- and p-semiconductors: t_n and t_p are the film thicknesses, d_n and d_p are the thicknesses of the space charges of n- and p-semiconductors; and I and U are the measuring current and potential contacts.

mately the same thickness but differed in the electron concentration. It is known [9–11] that the electrical conduction of undoped HgCr$_2$Se$_4$ crystals is due to mercury and selenium vacancies. In an as-grown crystal, p-type conduction is commonly observed. Both the conduction and the type of charge carriers can be modified by annealing in mercury vapor [9–11].

Parallelepipeds with sizes ~ (3.5–4) × (0.6–0.75) × (0.6–0.75) mm were cut from a large single crystal prepared by the gas transport method using the technique described in [12] and then polished. The samples were additionally annealed in sealed ampoules at an excess pressure of mercury vapor (from 0.5 to 10 atm) and a fixed temperature of 500°C for 30 min. After that, the samples were cooled at room temperature. Under these conditions, the modification of mercury vacancies will proceed within approximately the same effective thickness. It is known that for the diffusion processes the $p{-}n$ junction is not abrupt and the impurity concentration varies smoothly in the junction. It follows from our additional studies that, under the indicated conditions, mercury diffused mainly to a depth of about $l_d \approx 30{-}80$ μm.

The average values of the electrical resistivity ρ and the magnetoresistance MR$_H = [\rho(H) - \rho(0)]/\rho(H)$ were measured by the standard four-probe method. Indium leads were applied by an ultrasonic soldering iron to the surface of the layer annealed in mercury (Fig. 1).

It is seen (Fig. 2, curve 0) that the electrical resistivity in a homogeneous as-grown single crystal of p-HgCr$_2$Se$_4$ monotonically increases with decreasing temperature (activation energy $\Delta E \approx 0.2$ eV at $T \gg T_C$). The magnetoresistance is positive in the paramagnetic region and changes its sign slightly above the Curie temperature $T_C = 107$ K. The value of MR$_H$ is small and monotonically increases to maximum values MR$_H = -0.15$ at 77 K with decreasing temperature in the field $H = 15$ kOe (Fig. 3, right axis, curve 0). The results are typical of p-HgCr$_2$Se$_4$, and the nature of electrical resistance is principally understood (see [13]).
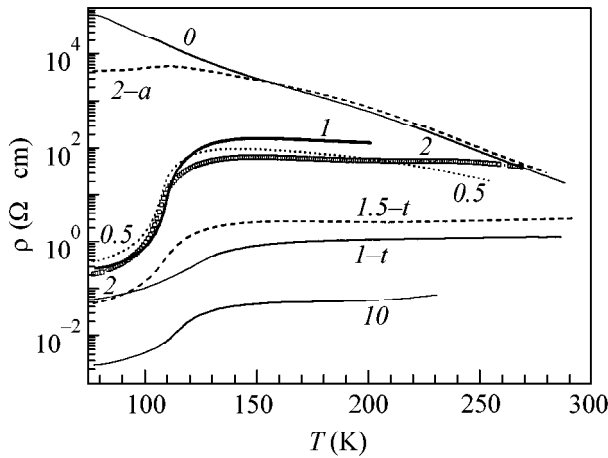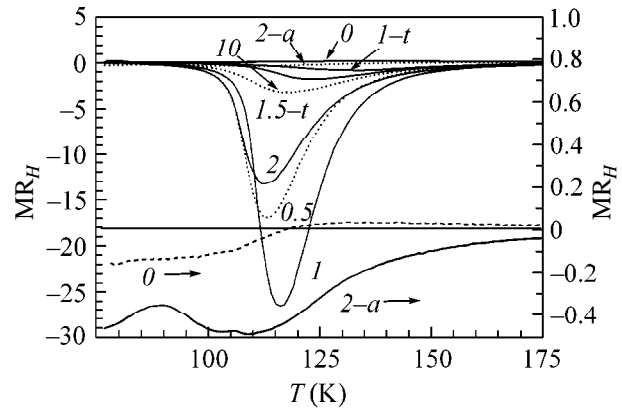
Fig. 2. Temperature dependences of the average electrical resistivity for the HgCr$_2$Se$_4$ samples annealed at various mercury vapor pressures. Numbers near the curves indicate the mercury vapor pressures in atm; letters at the numbers indicate that (*a*) the surface layer is removed and (*t*) the sample is thin (0.2–0.35 mm).

Fig. 3. Temperature dependence of magnetoresistance MR$_H$ = [ρ(*H*) – ρ(0)]/ρ(*H*) in a magnetic field of 15 kOe for the HgCr$_2$Se$_4$ samples annealed at various mercury vapor pressures. The values of MR$_H$ for two samples of HgCr$_2$Se$_4$ are scaled up on the right axis. Notations are as in Fig. 2.

All annealed samples exhibit below $T_C \approx 107$–117 K the metallic type of electrical conduction, evidencing the electronic type of conduction in the surface layer [10, 11]. We observed a 27-fold maximum decrease in the electrical resistivity (MR$_H \approx$ –27) for a sample annealed at 1 atm of mercury. MR$_H$ decreases with both decrease (0.5 atm) and increase (2 atm) in mercury vapor pressure from this value. On removing (by grinding) a ~100 μm-thick surface layer from a sample annealed at 2 atm, the MR$_H$ values and the electrical resistivity changed almost to those of the as-grown sample (Figs. 2, 3; curves *2, 2–a, 0*). Small differences in the ρ and MR$_H$ values can be explained by the diffusion of some amount of mercury into the deeper layers of the sample.

The electrical resistivities of an inhomogeneous sample of HgCr$_2$Se$_4$ annealed at 10 atm of mercury (Fig. 2, curve *10*) and a homogeneous sample of HgCr$_2$Se$_4$ annealed at 8 atm (Fig. 3, curve *1* [10]) are small (~10^{-3} Ω cm) and only slightly differ from each other. Due to the smallness of the ρ value (the concentration of charge carriers in the *n* layer is high [10]), electrons pass into the *p* layer from only a small part of the *n* layer, the contact-induced change in the volume of the conducting film is insignificant, and, accordingly, MR$_H$ is small.

A high MR$_H$ value observed in [10] for a HgCr$_2$Se$_4$ sample annealed at 1 atm of mercury is also noteworthy. In this connection, it might be assumed that the results obtained for electrical resistivity and magnetoresistance are not associated with the inhomogeneity of the sample but are caused by unknown reasons, for example, by the concentration effects in the mechanisms of electrical conduction in HgCr$_2$Se$_4$. For this

purpose, we performed annealing with thinner samples: 0.2 mm at 1 atm of mercury and 0.35 mm at 1.5 atm of mercury (Figs. 2, 3; curves *1–t, 1.5–t*). One can see (Figs. 2, 3; curves *1.5–t, 1–t*) that the MR$_H$ values significantly diminished, as compared to MR$_H$ for the thick (*t* = 0.6–0.75 mm) samples, and both MR$_H$ and electrical resistivity in sample *1–t* are smaller than in sample *1.5–t*. These results show that, under our experimental conditions, the depth of mercury diffusion and the thickness of the space charge *p*-HgCr$_2$Se$_4$ are approximately the same, $l_d \approx d_p \approx 30$–100 μm.

We also obtained direct evidence for the influence of surface phenomena on the electrical resistivity and magnetoresistance of the as-grown samples of HgCr$_2$Se$_4$. The electrical resistivity and the MR$_H$ values measured for the natural faces of HgCr$_2$Se$_4$ single crystals are much higher than those for crystal cuts. For one such sample, we found MR$_H$ = –350% in a magnetic field of 15 kOe in the vicinity of T_C. After removing a ~30–50 μm layer from the surface of the natural face, the value of MR$_H$ diminished from 350 to 10–20%. We believe that these results are explained by the fact that, according to the method of growing the HgCr$_2$Se$_4$ single crystals [12, 14], the ampoule contains an excess amount of mercury vapor. After switching off the furnace, a peculiar kind of annealing occurs in mercury vapor upon slow cooling of the sample and an inhomogeneous surface layer is formed.

These results give irrefutable evidence for the surface nature of magnetoresistance in HgCr$_2$Se$_4$. We believe that the $d(\text{MR}_H)/dH$ = 0.2%/Oe value attained in this work is not optimum and that the understanding of the nature of the phenomenon and the development of technology will allow it to be increased by at least one to two orders of magnitude.

Note in conclusion that the situation with magnetoresistance in lanthanum manganites is almost the same as in magnetic semiconductors [1]. Therefore, we believe that these conclusions also apply to lanthanum manganites, because these materials also exhibit some evidence for the influence of magnetic ordering on their band structure [15]. Evidently, one can also expect that the giant magnetoresistance values similar to those observed in some europium chalcogenides and chromium chalcogenide spinels (for example, EuO, EuSe, $CdCr_2Se_4$) [2] can also be obtained owing to the surface inhomogeneity of these magnetic semiconductors, because, in addition to the red-shift effect they exhibit transitions of the insulator–metal type upon changing vacancies [16].

Thus, the occurrence of inhomogeneous states (phase separation [1]) and the related contact phenomena (the appearance of a contact potential and a depletion layer at the interface between inhomogeneities; the exponential dependence of the charge-carrier concentration in the depletion layer on the contact potential U_c; and the dependence of U_c and the size of depletion layer on the magnetic field) can provide high magnetoresistance values.

REFERENCES

1. É. L. Nagaev, Usp. Fiz. Nauk **165**, 529 (1995) [Phys. Usp. **38**, 497 (1995)]; Usp. Fiz. Nauk **166**, 833 (1996) [Phys. Usp. **39**, 781 (1996)]; Fiz. Tverd. Tela (St. Petersburg) **40**, 2069 (1998) [Phys. Solid State **40**, 1873 (1998)].

2. S. von Molnar and S. Methffessel, J. Appl. Phys. **38**, 959 (1967); Y. Shapira, S. Foner, and T. B. Reed, Phys. Rev. B **8**, 2299 (1973); Y. Shapira, S. Foner, N. F. Oliveira, *et al.*, Phys. Rev. B **10**, 4765 (1974); K. P. Belov, L. I. Koroleva, and L. N. Tovmasyan, Zh. Éksp. Teor. Fiz. **73**, 2309 (1977) [Sov. Phys. JETP **46**, 1208 (1977)]; N. I. Solin and N. M. Chebotaev, Fiz. Tverd. Tela (St. Petersburg) **39**, 848 (1997) [Phys. Solid State **39**, 754 (1997)].

3. S. Jin, T. H. Tiefel, M. McCormack, *et al.*, Science **264**, 413 (1994); I. Panagiotopoulos, C. Christides, D. Niarchos, and H. Pissas, J. Appl. Phys. **87**, 3926 (2000).

4. V. M. Loktev and Yu. G. Pogorelov, Fiz. Nizk. Temp. **26**, 231 (2000) [Low Temp. Phys. **26**, 171 (2000)].

5. R. A. Smith, *Semiconductors* (Cambridge Univ. Press, Cambridge, 1959; Inostrannaya Literatura, Moscow, 1962).

6. N. I. Solin, S. V. Naumov, and A. A. Samokhvalov, Fiz. Tverd. Tela (St. Petersburg) **40**, 1881 (1998) [Phys. Solid State **40**, 1706 (1998)]; Fiz. Tverd. Tela (St. Petersburg) **42**, 899 (2000) [Phys. Solid State **42**, 925 (2000)].

7. J. Smit and H. P. J. Wijn, *Ferrites* (Wiley, New York, 1959; Inostrannaya Literatura, Moscow, 1962).

8. G. Busch and P. Wachter, Phys. Kondens. Mater. **5**, 232 (1966); T. Arai *et al.*, J. Phys. Soc. Jpn. **34**, 66 (1973).

9. V. G. Veselago, K. M. Golant, I. S. Kovaleva, *et al.*, Zh. Éksp. Teor. Fiz. **87**, 1857 (1984) [Sov. Phys. JETP **60**, 1068 (1984)].

10. L. Goldstein, P. Gibart, and A. Selmi, J. Appl. Phys. **49**, 1474 (1978).

11. A. Selmi, A. Mauger, and M. Heritier, J. Magn. Magn. Mater. **66**, 295 (1987).

12. N. M. Chebotaev, M. I. Simonova, T. I. Arbuzova, *et al.*, Izv. Akad. Nauk SSSR, Neorg. Mater. **21**, 1468 (1985).

13. M. I. Auslender and N. G. Bebenin, Solid State Commun. **69**, 761 (1989); V. A. Kostylev, B. A. Gizhevskii, A. A. Samokhvalov, *et al.*, Phys. Status Solidi B **158**, 307 (1990); V. A. Kostylev, B. A. Gizhevskiĭ, A. A. Samokhvalov, *et al.*, Fiz. Tverd. Tela (Leningrad) **32**, 38 (1990) [Sov. Phys. Solid State **32**, 20 (1990)].

14. P. Gibart, J. Cryst. Growth **43**, 21 (1978).

15. Y. Okimoto *et al.*, Phys. Rev. Lett. **75**, 109 (1995); R. V. Demin, L. I. Koroleva, and A. M. Balbashov, Pis'ma Zh. Éksp. Teor. Fiz. **70**, 303 (1999) [JETP Lett. **70**, 314 (1999)].

16. E. A. Nagaev, *Physics of Magnetic Semiconductors* (Nauka, Moscow, 1979).

Translated by A. Bagatur'yants

Magnetic Susceptibility of Noninteracting Fermions in a Confined Geometry

A. R. Minnullin and D. A. Tayurskiĭ

Kazan State University, ul. Lenina 18, Kazan, 420008 Tatarstan, Russia

Received November 13, 2000; in final form, November 21, 2000

A model system of an ideal gas of neutral fermions in a confined geometry of different symmetry and size is theoretically examined. The behavior of these systems is found to exhibit qualitatively new features such as the oscillations in magnetic susceptibility with changing geometry size and particle density, indicating that the geometric confinement substantially affects the thermodynamic properties of the system. © *2000 MAIK "Nauka/Interperiodica".*

PACS numbers: 75.40.Gb; 67.55.Cx; 71.10.Ay

1. Continuity of an energy spectrum is an acceptable approximation for macroscopic systems at high temperatures. For finite systems, the energy discreteness leads to important consequences at low temperatures. In particular, it is well known that the geometrically confined system of fermions acquires a number of new, often quite unexpected properties. Interest in problems of this kind arose long ago in connection with the investigation of metallic nanoparticles [1–6] and properties of atomic nuclei (see, e.g., [7, 8]). Progress in nanotechnology has stimulated study of the size effect on the properties of finite Bose and Fermi systems (see, e.g., [9] and references therein). In recent years, considerable interest has been shown in the physical properties of quantum liquids—liquid ^{3}He and liquid ^{4}He—in a confined geometry. Investigations of these liquids in pores of solids (see, e.g., [10, 11]) and the mesoscopic droplets of liquid ^{3}He in solid ^{4}He [12] testify to the new features in the behavior of these liquids under such conditions.

It should be noted that the results of previous studies of finite Fermi systems cannot be directly applied to liquid ^{3}He because neither the Coulomb and electron spin–orbit interactions, which are responsible for the properties of conduction electrons in metallic nanoparticles, nor the strong nucleon–nucleon interaction, which governs the properties of nuclear matter, are present in it.

The work [13], where the transport coefficients were studied for the case where the mean free path of quasiparticles is comparable with the system size, is an example of using the Landau Fermi-liquid theory in the investigation of the properties of liquid ^{3}He in a confined geometry.

When analyzing the effect of finite geometry on the properties of liquid ^{3}He, one should apparently distinguish between two causes for the appearance of new properties, as compared to the bulk liquid:

(i) "Purely geometric" factor—the presence of a geometric boundary modifies the energy spectrum of even noninteracting fermions;

(ii) "Fermi-liquid" factor—the Landau or any other Fermi-liquid theory should be reformulated for the confined geometry because the system size strongly affects the spectrum of elementary excitations.

The influence of the first factor was demonstrated in our work [14], where a model describing the effect of confined geometry (microcracks on a crystal surface) on the magnetic relaxation was proposed to explain the unexpectedly fast magnetic relaxation of liquid ^{3}He contacting dielectric van Vleck crystals or their diamagnetic analogues. The basic idea of this model is as follows. In a solid, where the translational motion of atoms is absent, the magnetic resonance line is rather broad and the transverse relaxation times are small. In a liquid, due to the translational motion of atoms, the resonance line is strongly narrowed, while the relaxation times are long. If a liquid where the modulation of dipole–dipole interaction by the diffusion motion is an efficient relaxation mechanism is placed in a confined geometry, not all diffusion modes are possible, in contrast to the bulk liquid, but only the resonant modes "survive." Therefore, the magnetic resonance line will not be as narrow as in the bulk liquid and, at the same time, as broad as in a solid. In the quantum liquid (liquid ^{3}He), the restrictions on the diffusion motion can be even more numerous, e.g., due to the Pauli exclusion principle. Numerical calculations for the spherically symmetric confined geometry corroborate these quali-

tative considerations and yield a difference of at least an order of magnitude between the longitudinal and transverse relaxation times for liquid ^{3}He [14, 15].

In this work, we will demonstrate how the geometric confinement leads to the appearance of new physical properties in a system of noninteracting fermions (gaseous ^{3}He and dilute quantum mixtures of ^{3}He in ^{4}He). In particular, the magnetic susceptibility of such a system becomes an oscillating function of the size or the particle number density. This resembles the well-known de Haas–van Alphen effect caused by the quantization of Landau levels in the electron gas in metals.

The inclusion of a real interaction between ^{3}He atoms in the form of, e.g., Aziz potential [16] will be the subject of our further investigations.

2. Due to the discreteness of states, the thermodynamic characteristics of finite systems, such as heat capacity and magnetic susceptibility, differ considerably from the corresponding macroscopic parameters. The mean spacing δ between the one-particle states in a finite system is on the order of E_F/N, where E_F is the Fermi energy and N is the number of particles. If the thermal energy kT or the Zeeman energy μH of a particle in an external magnetic field H (μ is the magnetic moment of the particle) or any other characteristic energy becomes of the order of δ or less, the discrete character of levels starts to influence the respective thermodynamic characteristics. Since the properties of Fermi systems are determined by the density of energy states at the Fermi level, further analysis of the effect of level discreteness on the thermodynamic properties requires certain assumptions about the distribution of energy levels near the Fermi energy [3].

However, the effects of confined geometry in a system of neutral fermions can be studied by using another approach that is based on the determination of the energy spectrum of particles by solving the corresponding Schrödinger equation and subsequent analysis of the thermodynamic and magnetic properties of these systems.

The effects of confined geometry can be most simply demonstrated for a system of N noninteracting fermions confined to a sphere of radius R. This geometry is implemented in the experiments with mesoscopic droplets of liquid ^{3}He in solid ^{4}He [12]. Evidently, droplets of liquid ^{3}He cannot be treated as a gas of noninteracting ^{3}He atoms and, as is mentioned above, the Landau Fermi-liquid approach should also be revised because of the changes in the spectrum of elementary excitations caused by the confined geometry. Nevertheless, manifestations of the confined geometry in the system of noninteracting fermions are of interest as a first approximation to the real situation.

In the case of interest, the energy spectrum of the particles (without regard for spin degeneracy) has the form

$$E_{l,n} = \frac{\hbar^2}{2m} k_{l,n}^2, \qquad (1)$$

where m is the mass of the particle (^{3}He atom in our case) and $k_{l,n}$ are found from the equation for the zeroes of the Bessel function

$$J_{l+\frac{1}{2}}(kR) = 0. \qquad (2)$$

The Bessel function for each l has an infinitely large number of zeroes, numbered by the subscript n. Since l is the orbital angular momentum of the particle, each energy level $E_{n,l}$ is $(2l + 1)$-fold degenerate and, thus, is strongly degenerate at large l values. This degeneracy can be removed by an external magnetic field. In addition, the symmetry lowering (e.g., to cubic or axial) due to the confined geometry also removes the degeneracy of energy levels. In our calculations of the thermodynamic and magnetic characteristics of a gas of noninteracting fermions confined to the spherical geometry, we numerically found zeroes of the Bessel functions, the maximum number of zeroes not exceeding 500. This allowed the consideration of the systems with sizes of up to 100 Å and particle number of up to 100000. Using the calculated zeroes of the Bessel functions, the energy spectrum can be rewritten as E_i, where i numbers the states in the order of increasing energy.

The Fermi energy E_F and the population n_i of each level at temperature T are determined in the usual way,

$$N = \sum_i \frac{1}{\exp((E_i - E_F)/kT) + 1}, \qquad (3)$$

$$n_i = \frac{1}{\exp((E_i - E_F)/kT) + 1}. \qquad (4)$$

The calculated Fermi energies and the density of states at the Fermi level are presented in the table for different radii of spherical geometry (in the numerical calculations, the particle density was taken to be $1.62 \times 10^{28} \, \text{m}^{-3}$, which corresponds to liquid ^{3}He at zero pressure). As the sphere radius increases, the Fermi energy monotonically decreases tending to a value of 5 K, which is

Fermi energy and density of states of a Fermi gas confined to a sphere of radius R. The particle density is equal to the density of atoms of liquid ^{3}He at zero pressure
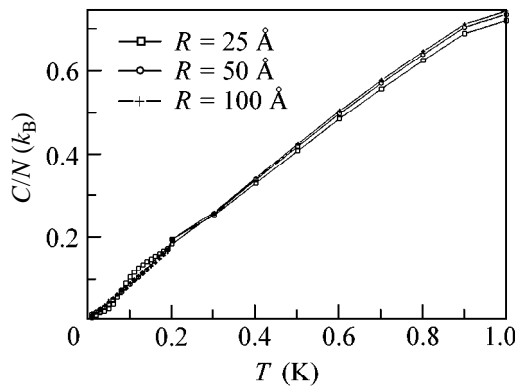
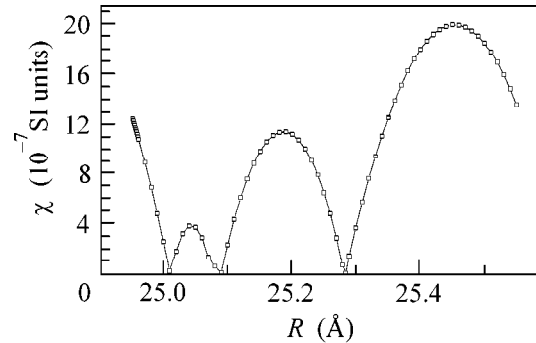| R, Å	E_F, K	Density of states, 1/K
25	6.01	170
50	5.87	1200
100	5.71	10000
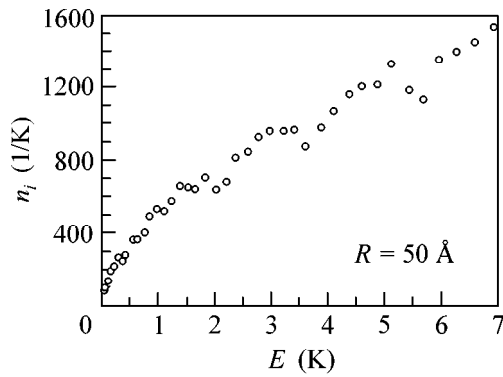
Fig. 1. Energy dependence of the density of states for a Fermi gas confined to a sphere of radius $R = 50$ Å. The particle density is equal to the density of atoms of liquid ^{3}He at zero pressure.
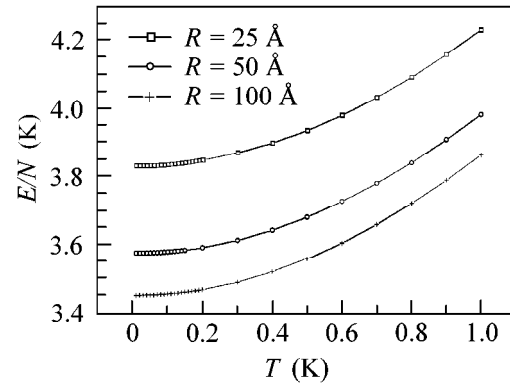
Fig. 2. Temperature dependence of the energy per one particle for the spheres of different radii.

Fig. 3. Temperature dependence of the heat capacity per one particle for the spheres of different radii.

Fig. 4. The magnetic susceptibility vs. the sphere radius.

obtained when treating bulk liquid ^{3}He as a gas of noninteracting Fermi particles. The energy dependence of the density of states is shown in Fig. 1 for a sphere of radius 50 Å. The oscillatory character of this dependence is clearly seen. Therefore, one should expect oscillations in the observable physical characteristics of the system.

Figures 2 and 3 show the temperature dependences of the energy per particle and of the heat capacity of a Fermi gas confined to spheres of various radii. Notice that the heat capacity in the approximation of noninteracting particles does not depend on the size of confined geometry and exhibits linear temperature dependence at temperatures below 0.5 K (which corresponds to approximately $0.1T_F$). Our calculations demonstrate that such a behavior holds also for the other shapes of confined geometry, e.g., for a cube.

As is mentioned above, due to the nonmonotonic energy dependence of the density of states, one can expect an appearance of oscillations in the physical characteristics of a confined gas of noninteracting Fermi particles. To demonstrate this, we calculated the

magnetic susceptibility for this gas as a function of temperature, particle density, and sizes of confined geometry. The magnetic susceptibility in the magnetic field H is calculated as

$$\chi = \frac{\gamma \hbar}{2} \frac{\sum (n_{i,\uparrow} - n_{i,\downarrow})}{VH}, \qquad (5)$$

where the level populations $n_{i,\uparrow(\downarrow)}$, with allowance made for spin, are

$$n_{i,\uparrow(\downarrow)} = \frac{1}{\exp\left(\dfrac{E_i - E_F - (+)\frac{1}{2}\gamma \hbar H}{kT}\right) + 1}. \qquad (6)$$

Here, γ is the nuclear gyromagnetic ratio of ^{3}He; $\gamma/2\pi = 3.24$ kHz/Oe. The oscillatory dependence of the magnetic susceptibility on the radius sphere is most interesting (Fig. 4). Such a behavior of the susceptibility at low temperatures can be easily understood from the following considerations. At very low temperatures, the
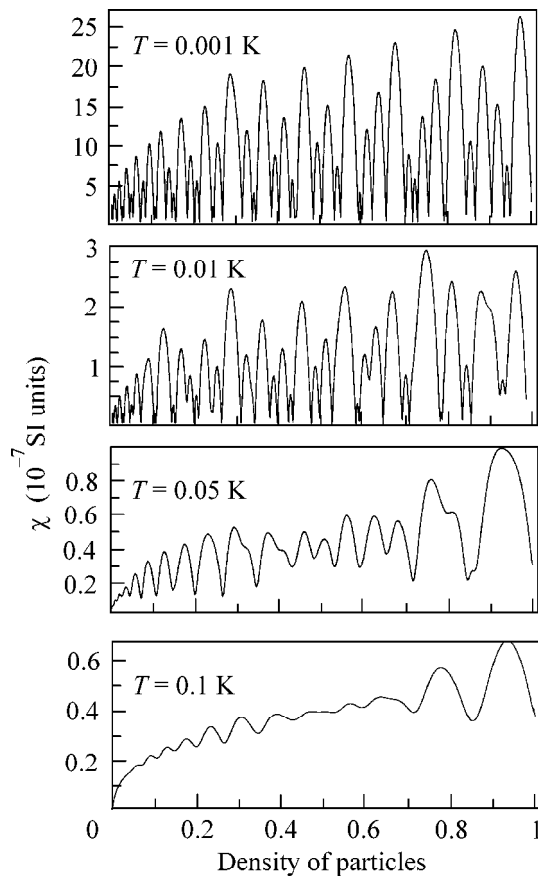
Fig. 5. The magnetic susceptibility vs. the density of particles at various temperatures for a sphere of radius 25 Å.

susceptibility, as also the magnetization, is determined by the particles at the nearest-to-E_F energy level. Let us assume that this level is $2(2l + 1)$-fold degenerate (with allowance made for the spin degeneracy) and there are n particles on this level. In a weak magnetic field, the susceptibility of this system satisfies the Curie law and is proportional to the difference between the numbers of particles with opposite spin projections (we consider particles with spin 1/2). The susceptibility is maximum at $n = l$ and decreases as n approaches zero or $2l$. Such a behavior, in a sense, is similar to the de Haas–van Alphen oscillations in electron gas with quantized Landau levels.

Of course, it is not practical to vary the radius of confined geometry under the experimental conditions and, hence, observe these oscillations. However, the density of accessible states depends also on the particle density which can easily be varied, e.g., in experiments with dilute ^3He–^4He solutions. The oscillations in the magnetic susceptibility with changing the density of Fermi particles at various temperatures are shown in Fig. 5 for the sphere of radius 25 Å. As the temperature increases, the oscillations are blurred because of

spreading the particle distribution over the energy levels near the Fermi level.

Our calculations show that for the confined geometry of lower (axial) symmetry (typical, e.g., of the experiments with liquid ^3He in Vycor glass [10, 17]) these oscillations strengthen and a modulation appears whose origin is yet to be clarified.

Note that recent experiments on the observation of the "expelling" of quasiparticles of liquid ^3He from the pores of Vycor glass with a decrease in temperature [17] were also explained by the confinement-induced change in the density of states at the Fermi level. A "semisuperfluidity" of liquid ^3He in aerogel, recently discovered in [18], also testifies to a considerable change in the magnetic and orbital states of ^3He in aerogel. Thus, further theoretical investigations of the effect of geometric confinement on the properties of Fermi systems seem to be quite topical.

To illustrate the effect of confined geometry on the properties of a system of neutral Fermi particles, we have considered in this study the model problem of an ideal Fermi gas confined to a sphere, cube, and cylinder of various sizes. These systems exhibit some effects, such as the oscillations in magnetic susceptibility with changing particle density, which indicate that the confined geometry gives rise to the essentially new features in the behavior of even the ideal systems. Evidently, the inclusion of a real interaction between the neutral Fermi particles will approximate the experimental conditions occurring in the studies of liquid ^3He in the confined geometry. This is the subject of our further investigations.

REFERENCES

1. R. Kubo, J. Phys. Soc. Jpn. **17**, 975 (1962).
2. A. Kawabata, J. Phys. Soc. Jpn. **29**, 902 (1970).
3. R. Denton, B. Mühschlegel, and D. J. Scalapino, Phys. Rev. B **7**, 3589 (1973).
4. J. Barojas, E. Cota, E. Blastein-Barojas, *et al.*, Ann. Phys. **107**, 95 (1977).
5. E. Blastein-Barojas, J. Flores, P. A. Mello, *et al.*, Phys. Lett. A **61**, 146 (1977).
6. G. M. Pastor, R. Hirsch, and B. Mühlschlegel, Phys. Rev. **53**, 10382 (1996).
7. A. B. Migdal and A. I. Larkin, Nucl. Phys. **51**, 561 (1964).
8. A. B. Migdal, *Theory of Finite Fermi Systems and Applications to Atomic Nuclei* (Nauka, Moscow, 1983, 2nd ed.; Interscience, New York, 1967).
9. D. V. Anghel, cond-mat/0006430.

10. B. N. Engel, G. G. Ihas, and G. F. Spencer, Can. J. Phys. **65**, 1545 (1987).

11. R. Schrenk and R. König, Phys. Rev. B **57**, 8518 (1998).

12. R. Schrenk, R. König, and F. Pobell, Phys. Rev. Lett. **76**, 2945 (1996).

13. M. J. Rice, Phys. Rev. **165**, 288 (1968).

14. V. V. Naletov, M. S. Tagirov, D. A. Tayurskiĭ, and M. A. Teplov, Zh. Éksp. Teor. Fiz. **108**, 577 (1995) [JETP **81**, 311 (1995)].

15. D. A. Tayurskii, in *Extended Abstracts of the XXVII Congress AMPERE, Kazan, 1994*, p. 219.

16. R. A. Aziz, V. P. S. Nain, J. S. Carley, *et al.*, J. Chem. Phys. **70**, 4330 (1979).

17. P. A. Reeves, A. M. Guénault, S. N. Fisher, *et al.*, Physica B (Amsterdam) **284–288**, 319 (2000).

18. Yu. M. Bunkov, A. S. Chen, D. J. Cousins, and H. Godfrin, Phys. Rev. Lett. **85**, 3456 (2000).

Translated by R. Tyapaev

To the Memory of Our Contributors

PACS numbers: 01.60.+q

I.M. Beterov *et al.*, **Experimental Implementation of a Four-Level N-Type Scheme for the Observation of Electromagnetically Induced Transparency** [JETP Lett. **71**, 175 (2000)].

Igor' Mendelevich Beterov, doctor of physics and mathematics, professor, director of the Quantum Electronics Division at the Institute of Semiconductor Physics, Siberian Division, Russian Academy of Sciences, suddenly died September 3, 1999.

Beterov was born June 7, 1942, in Ordzhonikidze. After graduation from the Novosibirsk State University in 1964, he took a position at the Institute of Semiconductor Physics, Siberian Division, USSR Academy of Sciences. He progressed from a senior laboratory worker to the director of the division, combining his work at the institute with teaching activity.

Beterov will be kept in colleagues' memory as an outstanding experimenter. He developed original methods of studying atomic photoionization processes, for polarization nonlinear spectroscopy, and for infrared and microwave spectroscopy of highly excited (Rydberg) states. Beterov pioneered the studies of three-level systems, one of the main present-day objectives of laser spectroscopy. His works on tunable lasers, laser studies of surface phenomena, and investigations into multiphoton processes in atomic gases are widely known.

Beterov was an organizer of several Vavilov Conferences on Nonlinear Optics, held at the Novosibirsk Akademgorodok, as well as International Conferences and Workshops on Quantum Electronics. He was a member of the SPIE and the Rozhdestvenskiĭ Optical Society.

The Beterov's achievements will remain a good memory of this remarkable scientist and man. Prof. Beterov's death is a great and irreparable loss for his collaborators and colleagues.

V.I. Mikhaĭlichenko *et al.*, **Experimental Study of the Subthreshold Production of K^+-Mesons in Proton–Nucleus Collisions** [JETP Lett. **72**, 100 (2000)].

Vyacheslav Ivanovich Mikhaĭlichenko, leading scientific researcher of the Institute of Theoretical and Experimental Physics, candidate of physics and mathematics, suddenly died at the age of 61. After graduation from the Moscow Institute of Engineering Physics, he joined the laboratory of S.Ya. Nikitin at the Institute of Theoretical and Experimental Physics, where he worked all his life. Mikhaĭlichenko organized data processing from the USSR's greatest two-meter liquid-hydrogen bubble chamber and controlled all the results obtained on it. He initiated interesting research into physics of baryon and meson resonances involving strange particles. In his final years, he participated in the work of a research group on studying the subthreshold production of K mesons by nuclei and has made a considerable contribution thanks to his erudition and professionalism. The good memory of Mikhaĭlichenko will be kept for a long time in the hearts of his numerous friends and collaborators.

Translated by V. Sakun